# Textural Variability Using the ZEISS Arivis Cloud Tool - Sosa Dyke, Neuquén

## Potential of Object-Based Segmentation on Petrographic Thin Sections

AESB3400: Bachelor Thesis

A.D. Hoogeveen

TUDelft

# Textural Variability Using the ZEISS Arivis Cloud Tool - Sosa Dyke, Neuquén

## Potential of Object-Based Segmentation on Petrographic Thin Sections

by

## A.D. Hoogeveen

To obtain the degree of Bachelor of Science at the
Delft University of Technology, to be defended
publicly on 9 April 2025

| | | |
|---|---|---|
| **Student Number:** | 5512980 | |
| **Thesis Committee:** | Dr. T. Schmiedel | TU Delft, Supervisor |
| | J.C. Blom | TU Delft, Supervisor |
| **Project Duration:** | February 2025 – April 2025 | |
| **Faculty:** | Faculty of Civil Engineering and Geosciences, Delft | |

**TU**Delft

# Abstract

Analysis of petrographic thin sections is crucial to determine rock properties such as texture, crystal size distribution, porosity and structure of rocks at a microscopic level. However, an accurate determination of minerals and textures in petrographic thin sections is a time-consuming process. Despite efficiency improvements through intensity-based segmentation, thin section petrography remains slow and manual, leaving a significant amount of sections unexamined due to time constraints. This project aims to determine whether object-based segmentation can be used to segment similar mineral phases in petrographic thin sections using the AI-driven ZEISS arivis Cloud (formerly APEER).

Samples used in this project were collected by the authors of Schmiedel et al. (2021) across a traverse of the high viscosity Sosa Dyke (37°2'S, 68°52'W) in Argentina. Ten thin sections of trachyte/trachydacite composition were scanned under bright light (BL), circularly polarized light (CPL), cross-polarized light (XPL) and plane-polarized light (PPL) using the ZEISS Axioscan 7 and provided to be used in this project.

The effects of annotation quantity, image resolution and the combination of CPL and BL images in a single model were investigated through the creation of multiple AI segmentation models using arivis Cloud. Additionally, the time spent on segmentation was compared to intensity-based segmentation, point counting, and manual segmentation. The classes used to segment images were amphiboles, plagioclase, and opaque minerals.

Results from this project show that ZEISS arivis Cloud can be used to segment thin sections using object-based AI models. Object-based segmentation with ZEISS arivis Cloud is shown to be more time-efficient than other manual and intensity-based segmentation methods. Larger datasets of similar thin sections result in greater time savings, and the platform also generates valuable data which can be used for geologic interpretation. BL images produced more accurate models than CPL images, and increased annotation of images improves model accuracy. Models trained on higher resolution images more accurately differentiated between plagioclase and amphiboles. Conversely, higher resolution models were less consistent in identifying large plagioclase crystals. Annotation bias and arivis Cloud performing optimally when objects are no larger than 320*320 could be reasons for this. Although contradictory to the recommendations of the arivis Cloud documentation, combining BL and CPL images into a single model may improve segmentation accuracy when applied to BL images.

If fully optimized, ZEISS arivis Cloud could become an important tool for analyzing thin sections that were previously deemed too time consuming, potentially unlocking new geologic insights.

# Contents

# Nomenclature

## Abbreviations

| Abbreviation | Definition |
| --- | --- |
| BL | Bright Light |
| CSD | Crystal Size Distribution |
| CPL | Circularly Polarized |
| PPL | Plane Polarized Light |
| XPL | Cross Polarized LIght |

# 1
# Introduction

Analysis of petrographic thin sections are crucial to determine rock properties such as texture, crystal size distribution, porosity and structure of rocks at a microscopic level. However, an accurate determination of minerals and textures in petrographic thin sections is often a time consuming process. Since the introduction of thin section petrography by Henry Clifton Sorby in 1849, advancements such as intensity-based image analysis have improved efficiency [5, 27]. Despite this, thin section petrography remains a slow and manual process, resulting in a significant amount of sections remaining unexamined due to time required for analysis.

AI-driven tools have the potential to accelerate this process process. One such tool is ZEISS arivis Cloud (previously APEER), which is a cloud-based platform primarily used in medical applications [8, 11]. Currently, no studies have investigated the use of arivis Cloud for instance (object) based segmentation of mineral phases in petrographic thin sections. The aim of this project is to determine whether object-based segmentation using ZEISS arivis Cloud can be used to segment similar mineral phases with different textural parameters (e.g. crystal size, different matrix composition, different degree of fractionation) in petrographic thin sections.

The 10 thin sections analyzed in this project were taken from a traverse of the Sosa Dyke (37°2'S, 68°52'W) in the Neuquén Basin, Argentina by the authors of Schmiedel et al. (2021). The sections were scanned under BL, CPL, XPL, and PPL using the ZEISS Axioscan 7. Previous work on this dyke includes studies by Nilsson (2020), Schmiedel et al. (2021), and Palma et al. (2024) focused on large-scale features to investigate the emplacement mechanisms of the dyke. If proven useful, arivis Cloud segmentations could provide insights into the micro-textural and mineralogical causes of these large scale features in a potentially more time-efficient manner than manual image analysis methods.

The following aspects were investigated to determine the applicability of arivis Cloud.

- How does the use of ZEISS arivis Cloud compare to more traditional segmentation methods in terms of time efficiency?
- What effect does the number of annotations have on segmentation?
- What effect does image resolution have on segmentation?
- Does combining BL and CPL images into one model improve segmentation accuracy?

This report begins with an overview of the geologic setting of the Sosa Dyke, and a discussion of dyke formation theory. The Methods section describes how the arivis Cloud platform was used, and provides details on the models that were created. The results display figures and tables illustrating the impact of annotations, image resolutions and combining BL and CPL images, as well as examples of output data which could be used for geologic interpretation. In addition, a time comparison is done between traditional image analysis methods and the arivis Cloud segmentation. In the discussion section, the results will be analysed and related to the research question. The conclusion provides a summary and recommendations for further research and the potential use of arivis Cloud.

# Geologic Background

## 2.1. Geologic Setting

Samples used in this project were taken from the Sosa dyke, a high viscosity dyke that is part of the Chachahuén volcano complex [23]. The volcano is part of the Payenia volcanic province, a Cenozoic back-arc region, resulting from the Nazca plate subducting beneath the South American plate. [14, 20, 23]. The Payenia volcanic province is located within the older Neuquén foreland basin which has been a sedimentary sink from the Early Triassic to present day [7].

The Chachauén Volcanic Complex has produced volcanic rocks of varying composition beginning in the Early Miocene with basalts produced by fissure eruptions. In the late Miocene, ignimbrites and block-and-ash flows rocks characterize the majority of deposits in the Chachahuén edifice [23]. The Sosa Dyke is an intrusion into these deposits. In this period cryptodomes formed. Subsequently, most of these collapsed. One of the few that did not is the Cerro Bayo cryptodome (6.7 $\pm$ 0.3 Ma). The Sosa Dyke is located to the east of Cerro Bayo [23].
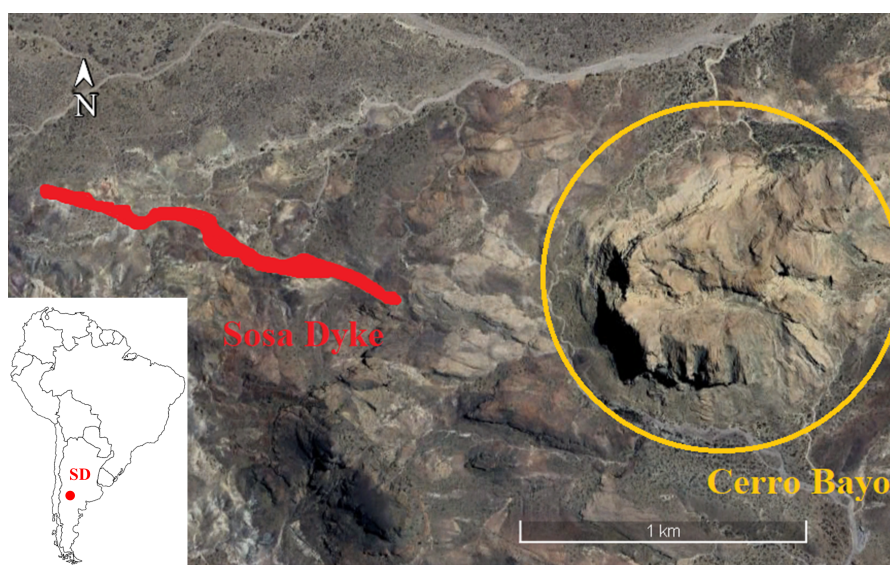


**Figure 2.1:** Location of the Sosa Dyke (SD). Dyke is located at 37°2'S, 68°52'W, to the east of the Cerro Bayo cryptodome (source: Google Earth), and its position in South America (modified from https://www.nicepng.com).

## 2.2. Dykes and Theory

Magma-filled fractures that cut across bedding planes, in both fluid and frozen states, are referred to as dykes. Dykes are an essential element of volcanic plumbing systems and are considered a major pathway for magma transport from the middle to upper path of the crust [6, 15].

Dykes transport magma to feed volcanic eruptions. However, if magma does not reach the surface, it solidifies and crystallizes in the subsurface. The largest temperature difference occurs at the dyke margin. Crystallization begins here and propagates towards the center of the dyke [15]. Following from this, solidified dykes can provide a valuable insight into variations in flow direction within the dyke over time as crystallization occurs. These flow directions can be highly variable. Interpretation is possible through analysis of magnetic fabrics and macroscopic textures like flow banding, folding, and phenocryst alignment [13, 15].

## 2.3. Sosa Dyke

The exposed part of the Sosa Dyke which was studied by Schmiedel et al. (2021) solidified in the subsurface. The dyke has a total length of about 1300 m measured along the strike (average orientation of 277°) and is considered to be a vertical sheet [23]. Samples used in this project are from the easternmost section (segment I). It is 560 m long with an average thickness of about 42 m. The plane of the dyke is oriented at 299° in the section containing T1 [23]. The dyke has a trachyte/trachydacite composition with a slightly more mafic composition in the dyke center [23].
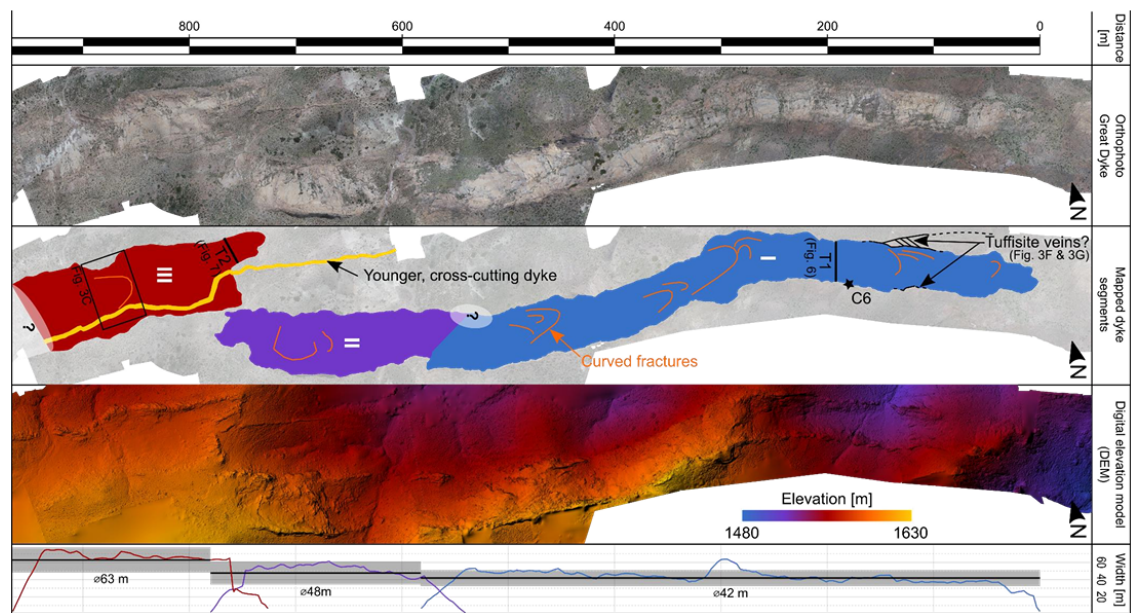


**Figure 2.2:** Figure 2 from Schmiedel et al. (2021). Overview of the Sosa Dyke. Samples used in this project are taken from traverse T1, located in the easternmost portion of the Sosa Dyke.
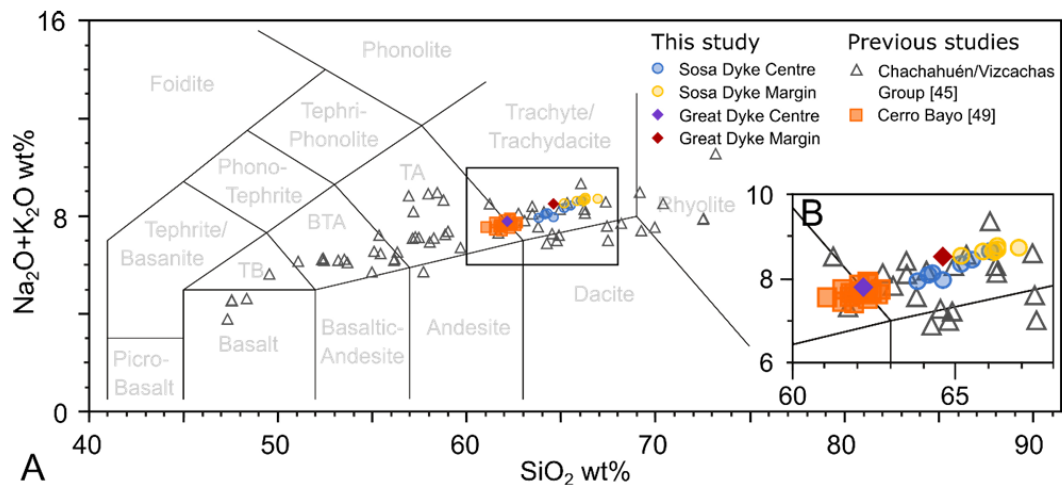


**Figure 2.3:** Figure 8 from Schmiedel et al. (2021). (**A**) Composition and classification of rocks for the Sosa Dyke (**B**) Zoomed portion of the figure.

# Methods

## 3.1. Input Data: Scanning Petrographic Thin Sections

The data used in this study was collected on site at traverse T1 of the Sosa Dyke by the authors of Schmiedel et al. 2021 (see Figure 2.2). In the study, nine cores were drilled at locations spaced 5 m apart (Figure 3.1) to measure AMS. At these same locations, rock samples were taken and labeled "GD-T1-01" to "GD-T1-09." The rock samples were used to create thin sections used in this project.

From these cores, 10 thin sections were created using clear epoxy. Sample GD-T1-09 is a special case. Here thin sections were created using a blue dye added to the epoxy to highlight potential porosity and enhance the visibility of clear minerals. In addition, two separate thin sections were made (GD-T1-09a and GD-T1-09b) oriented perpendicular to each other.

All sections were scanned using the ZEISS Axioscan 7 in combination with the ZEN (blue) microscopy software. Each sample was scanned under Plane Polarized light (PPL), Cross Polarized light (XPL) both at six intervals of 15 degrees, bright light (BL) and circularly polarized light (CPL). The scanning profile used can be found in the digital appendix. Regular images of the thin sections with a scale bar were also provided and used to calculate pixel size for low and high resolution images.

For each sample, an area of interest was manually selected, resulting in slight variations in image resolutions. At full scanning resolution the file size was too large to export. Images were therefore exported at 10% resolution (low), and 25% resolution (high) of the initial resolution. The resolution of each image is listed in table 3.1. All images are .tif files with a bit depth of 24.



**Figure 3.1:** Figure 6 from Schmiedel et al. (2021). Sample locations across the Sosa Dyke with indicated magnetic lineation (arrows) and magnetic foliation (strike-dip symbols) Sample T1-09 is located 5 m left of sample T1-08.

| Sample | Low Resolution | High Resolution |
|---|---|---|
| GD-T1-01 | 4278x2469 | 10694x6171 |
| GD-T1-02 | 4463x3133 | 1157x7832 |
| GD-T1-03 | 5401x2918 | 13503x7295 |
| GD-T1-04 | 4585x2480 | 12144x6201 |
| GD-T1-05 | 5414x2479 | 13535x6197 |
| GD-T1-06 | 5043x2703 | 12608x6757 |
| GD-T1-07 | 5227x2924 | 13608x7310 |
| GD-T1-08 | 5574x2912 | 13935x7280 |
| GD-T1-09a | 4472x2027 | 11179x5067 |
| GD-T1-09b | 4658x1805 | 11645x4512 |

**Table 3.1:** Resolution (in pixels) of the images used in this study for each sample.

## 3.2. Training Arivis Cloud Models

To test the potential of object or instance based segmentation, the ZEISS arivis Cloud (previously known as APEER) software was used [8]. More specifically, the one month academia trial. This trial includes thirty days of access and 7020 minutes of computing time, of which 4000 minutes were used to create about 40 segmentations.

In this project, the use of the arivis Cloud to segment mineral phases consists of four steps; annotation, training, inspection and analysis. Each segmentation followed this general procedure.

First, the images to be annotated were uploaded into a dataset. The dataset was given a logical name, referring to the type of images within the dataset or the type of model which was going to be trained using the dataset. When creating the dataset, arivis gives the option between semantic (pixel-based) and instance (object-based) segmentation. In this project, instance segmentation was used.

Within the dataset, images can be annotated. Depending on the requirements of the model being created, annotations were created on one, several, or every image in the dataset. This information is listed in section 3.4.

Annotations must be created for classes of interest which are defined by the user. In this project the classes are are amphibole, opaque minerals and plagioclase.

Annotation was mostly done using the AI tool, which predicts the outline of the crystal when hovering over it. If the outer boundary is correctly identified, clicking on the prediction creates an annotation. If the predicted outline is not adequate, the annotated area can be adjusted using the brush and eraser tools.

Once annotation is complete, the AI model is trained by selecting an annotated dataset and the classes of interest. Training the model occurs on the cloud and uses computing time. For the models trained and segmentations created in this project, this took an average of about 100 minutes, ranging between one to four hours.

Once completed, it is possible to inspect the model's predictions on the annotated dataset. Annotation is an iterative process and can be done multiple times until the model performs adequately. The first iteration of a model is either not indicated or labeled as v1. Subsequent iterations are labeled with v2,v3 etc.

If, upon inspection of the model's predictions, the predictions are satisfactory, the segmentation results can be downloaded. This is in the form of a .ome file and a .csv file. Within the .ome file is a .tiff file for each class indicating the identified objects in grayscale. In the .csv file are measurements, done by arivis Cloud on the identified objects. This file is conveniently named measurements.csv. Some of the measurements include the centroid coordinates, object area and major axis length. A list of all measurements contained within .csv file can be found in appendix A.

In this project, either one (GD-T1-01), three (GD-T1-01, GD-T1-05, GD-T1-09a) or all ten images were segmented dependent on the purpose of the model. Segmenting all ten allows for comparison across the dyke.

Although PPL and XPL images were provided, BL and CPL contains less variation between images of the same sample and therefore provides more consistent data for the AI to train on [11]. Therefore, only BL and CPL images were used.

According to the arivis documentation the segmentation can be accessed through ZEISS software such as, ZEN, or ZEN core. I did not have the licenses for these products and therefore wrote a Python script (contained within the digital appendix) to handle the files and create outputs which can be interpreted. It is possible to integrate Python scripts using docker, however due to limited time with the platform this option was not explored.
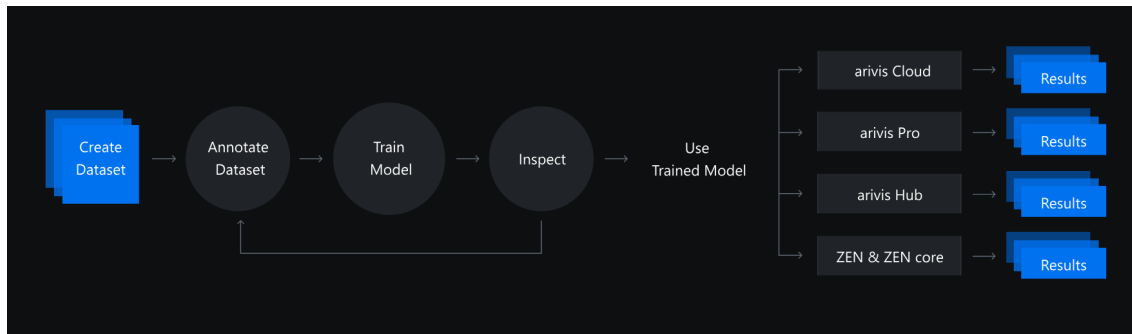


**Figure 3.2:** The AI model development overview from arivis Cloud [8]. In this project results are analyzed using Python.

## 3.3. Output Data using Python

The Python file created is attached in the digital appendix. As inputs the script takes a folder congaing the .ome files and the .csv file from arivis Cloud. The model name, image specifications, and names of colors for each class must be input manually. For the data in this project, the conversion done from pixels to $\mu$m was not accurate. For this reason, it is necessary to provide pixel size in $\mu$m per pixel. Additionally, users must specify the folders where the script will save the output files. In table 3.2 the output data is described.

Arivis considers the major axis orientation (radians) to be at the three o'clock position, and clockwise movement to be positive. For interpretation, it is more logical for the zero to be located at the twelve o'clock position. This is adjusted within the code.

| Output Data | Input Data | Description of Methods | Output File Type |
|---|---|---|---|
| Segmented Image | Folder containing .ome files. Each .ome consists of a greyscale .tiff file for each class | Convert each .tiff file into binary. Color by class and overlay. Creates one image per sample | .png or .tiff. |
| Major Axis Plot | measurements.csv | From the centroid coordinates, define line endpoints. Plot the major axis of each crystal. | .png |
| Orientation Rose Plots | measurements.csv | For each class, the histogram of orientations is plotted on a rose plot. | .png |
| Summary Excel File and Plot | measurements.csv | For measurements of interest, group data by class and by sample. Save to an Excel file and plot. | .xlsx and .png |
| Major Axis Length Violinplot | measurements.csv | Plot the major axis length for each class for comparison between models. | .png |
| CSD | measurements.csv | For each sample, cumulative probability for crystals of a given size is plotted against crystal size. Major axis length is used for crystal size. | .png |

**Table 3.2:** Output data created using Python which can be used for interpretation and analysis.

## 3.4. Comparison of Models

To determine the potential of object based segmentation using arivis Cloud, different variations of annotations and models were created for comparison.

### 3.4.1. Number of Annotations and Annotating Multiple Classes
The first set of annotations and models were trained to investigate the effects of the number and type of annotations. This followed the recommendations found in the arivis Cloud docs: annotate about 50 objects for a single class, inspect the results, identify areas of weakness, annotate more images and repeat until satisfied, the move on to the next class [11].

The first class which was annotated was plagioclase, starting with about 50 annotations on the low resolution (for specific resolutions refer to table 3.1) BL image of sample GD-T1-01 to create the first model; T1-01-bright10. The number of additional annotations created for iterations of this set of models are shown in table 3.3.

Note, this dataset included low resolution BL images of all samples (10 in total). Samples GD-T1-09a and GD-T1-09b are not annotated. These slides are used as test images to determine what effect the blue dye has on the predictions that the model makes.

| Model Name | Plagioclase Additional Annotations |
|---|---|
| T1-01-bright10v1 | 50 on GD-T1-01 |
| T1-01-bright10v2 | 300 on GD-T1-01 |
| T1-01-bright10v3 | 300 on GD-T1-05 |
| T1-01-bright10v4 | 50 on each unannotated sample, except GD-T1-09a and GD-T1-9b |
| **Total Annotations** | **950** |

**Table 3.3:** Additional annotations created for each model. Samples GD-T1-09a and GD-T1-9b were not annotated to determine how arivis Cloud deals with different thin section

After creating the annotations for plagioclase crystals, the other two classes were annotated (amphiboles and opaque minerals) in the same dataset to expand the model. First, amphiboles were annotated with 50 annotations on each image except GD-T1-09a and GD-T1-09b . This resulted in model T1-bright10_pav1.

Next, 50 opaque minerals were annotated on each image except GD-T1-09a and GD-T1-09b to create model T1-bright10_paov1. For an overview of the total number of annotations for T1-bright10_paov1 see table 3.4.

This model was used to segment all ten sample images.

| Class | T1-bright10_paov1 Total Annotations |
|---|---|
| Amphibole | 400 |
| Opaque | 400 |
| Plagioclase | 950 |

**Table 3.4:** Total number of annotations per class to create model T1-bright10_paov1

### 3.4.2. Resolution

According to arivis Cloud documentation the minimum image resolution is 128*128 pixels [11]. Images scanned using the Axioscan have much higher resolutions (see table 3.1). To determine the influence of image resolution on the AI models, images in BL and CPL were compared when trained on low and high resolution datasets.

In the model names, such as T1-bright10 or bright&cpl_25_v1, 10 and 25 refer to the percentage of the resolution of the initial scan. 10 refers to the to low resolution image and, 25 refers to the high resolution image as listed in 3.5.

Each dataset consists of all samples of the given resolution. The first sample GD-T1-01 was annotated with 50 objects for all three classes (amphibole, opaque, plagioclase). The model was then trained, resulting in predictions on every sample image. This allows for a visual comparison between the different models, as well as a statistical one.

| Model Names | Sample | Annotations per Class |
|---|---|---|
| Bright_10_resolution | GD-T1-01 | 50 |
| Bright_25_resolution | GD-T1-01 | 50 |
| CPL_10_resolution | GD-T1-01 | 50 |
| CPL_25_resolution | GD-T1-01 | 50 |

**Table 3.5:** Model names for the resolution tests and number of annotations per class on GD-T1-01.

### 3.4.3. Bright&CPL

This model is an investigation into whether it is possible to combine information from BL and CPL images into one model. For each model listed below, a dataset is created which contain both BL and CPL images.

Higher resolution images show more internal features, so this concept was tested for both low resolutions and high resolutions. For low resolutions, three model iterations were created bright&cpl_10_v1, bright&cpl_10_v2, and bright&cpl_10_v3. Iteration v2 and v3 included a total of 150 more annotations (50 per class) than the previous. For the high resolution images only one model was created: bright&cpl_25_v1.

To combine information from BL and CPL images, both must be annotated. To stay within time constraints, only samples GD-T1-01, GD-T1-05 and GD-T1-09a were used. These samples are located at the margin and center of the dyke and therefore display significant variation in textural parameters.

Table 3.6 shows the number of annotations created on both BL and CPL samples for each class for the associated model.

Model bright&cpl_10_v3 was used to segment all twenty low resolution images (BL and CPL).

| Model | Sample | Annotations per Class for BL and CPL |
|---|---|---|
| bright&cpl_10_v1 | GD-T1-01 | 50 |
| | GD-T1-05 | 0 |
| | GD-T1-09a | 0 |
| bright&cpl_10_v2 | GD-T1-01 | 50 |
| | GD-T1-05 | 25 |
| | GD-T1-09a | 0 |
| bright&cpl_10_v3 | GD-T1-01 | 50 |
| | GD-T1-05 | 25 |
| | GD-T1-09a | 25 |
| bright&cpl_25_v1 | GD-T1-01 | 50 |
| | GD-T1-05 | 0 |
| | GD-T1-09a | 0 |

**Table 3.6:** The number of annotations for each class on both BL and CPL samples per model.

### 3.4.4. High Resolution Models with Many Annotations

Previous models were created to investigate the effect of number of annotations, resolution, and image types. The models in this section were made to determine the effects of many annotations on high resolution images, potentially to create the the most accurate segmentation.

Models (see table 3.7) were created for both BL and CPL images with fifty annotations per class (amphibole, opaque and plagioclase) on each image. After creating the first iteration of both models, it became clear they had trouble predicting large plagioclase crystals so a second iteration was created with 10 extra annotations of large plagioclase crystals on each sample (total 100 extra annotations).

Since the thin sections for samples GD-T1-09a and GD-T1-09b were prepared using blue dye, it was deemed necessary to remove large blue areas from the AI's area of interest. This was done using the background class in arivis Cloud.

| Model | Sample | Annotations per Class for BL and CPL |
|---|---|---|
| Bright25-bestv1 | All Samples | 50 |
| Bright25-bestv2 | All Samples | 50 |
| | | + 10 extra for Plagioclase |
| CPL25-bestv1 | All Samples | 50 |
| CPL25-bestv2 | All Samples | 50 |
| | | + 10 extra for Plagioclase |
| **Total Annotations per Model** | | **1500-1600** |

**Table 3.7:** The number of annotations for each class on both 'best' models.

## 3.5. Time and Quality Comparison to Manual Segmentation Methods

To create a quantifiable indication of possible time saved using the arivis Cloud and to be able to make some comments on the quality of the data produced by arivis, a few manual segmentation methods were completed.

### 3.5.1. Traditional Intensity Based Segmentation using ImageJ

To compare the quality of the arivis object-based segmentation to an intensity-based segmentation, sample GD-T1-01 was segmented using ImageJ.

To segment each class the following procedure was completed three times. The image was converted to 8-bit (grayscale) and if deemed necessary, the contrast was increased. To segment the crystals the threshold function was used. The image was converted to a binary image. Possible noise was removed. The grain analysis tool was used to create measurements of the identified crystals. Using a modified version of the Python script, a colored segmented image was created.

The time required to segment all ten samples was found as follows.

$$T = t * n.$$

$T$: Total time used to manually segment the dataset, $t$: time to segment one sample using ImageJ, $n$: number of samples in the dataset.

### 3.5.2. Point Counting

Another method to acquire data from a petrographic thin section is point counting. Using ImageJ, a grid of 336 crosses was overlain over GD-T1-01. At the intersection of each cross, if there is a crystal, its long axis was measured. To create ellipsoids, the minor axis is also necessary. It is not measured, but time required to measure both axes can be extrapolated as follows.

$$T = 2 * t * n.$$

$T$: Total time used to manually segment the dataset, $t$: time to measure major axis length for one sample, $n$: number of samples in the dataset.

### 3.5.3. Manual Segmentation

For comparison, a quarter of the high resolution image of GD-T1-01 was segmented by hand. This was done using Goodnotes on an iPad with an Apple Pencil. The exact resolution of the segmented section was 7346x3085. By area, this is one quarter on the total image.

To extrapolate the amount of time taken for all ten images the following formula was used.

$$T = \frac{1}{p} * t * n.$$

$T$: Total time used to manually segment the dataset, $p$: fraction of sample area annotated, $t$: time to annotate fraction of sample area, $n$: number of samples in the dataset.

# 4

# Results

This chapter first compares the amount of time required to create an arivis Cloud segmentation as compared to other segmentation methods. Then, some examples of output data are displayed, followed by the results of models annotated with different parameters are shown.

## 4.1. Time Used and Comparison to Traditional Methods

This section details the time taken to segment images using arivis Cloud and the manual segmentation methods. The final comparison is displayed in Table 4.2.

### 4.1.1. Arivis Cloud

Uploading images, annotating and segmentation all take time. Uploading images and converting them for can take up to a few minutes per image, especially for larger resolution images. The time it takes per annotation depends on a few factors. How large the objects are, how identifiable they are, but mostly how well the AI tool can predict the boundaries of the image. If the AI tool does not predict the boundaries correctly, they must be manually adjusted. This occurs more frequently in objects with large contrast within the object. Taking this into account, I managed between 4-8 annotations per minute. Training and segmenting the models created in this project never took more than four hours. Usually, this took around two hours.

### 4.1.2. Traditional Intensity Based Segmentation Using ImageJ

Creating a segmentation of one image using ImageJ took about two hours (see Figure 4.1). Plagioclase and opaque minerals were easier to segment as they are in the upper and lower percentiles of grayscale values. Amphiboles' lower bound was similar to opaque minerals' upper bound. In addition, amphiboles upper bound had similar grayscale values to the matrix, resulting in few amphiboles detected as can be seen in Table 4.1.

| Class | Count | Segmented Area |
|---|---|---|
| Amphibole | 4209 | 1% |
| Opaque | 1121 | 3% |
| Plagioclase | 1943 | 25% |
| **Total** | **7273** | 28.5% |

**Table 4.1:** Number and percentage of GD-T1-01 segmented as amphibole, opaque, and plagioclase using ImageJ.
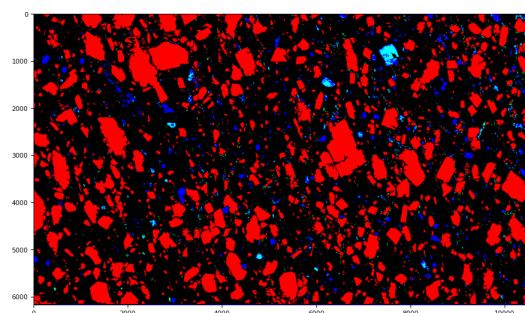


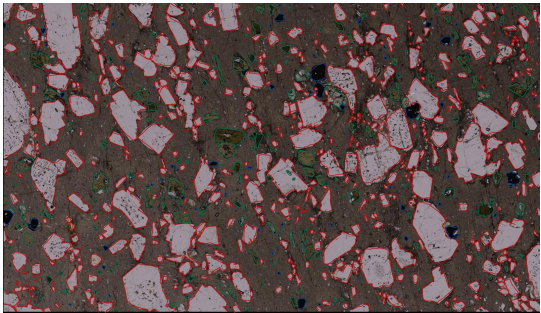**Figure 4.1:** Segmentation of GD-T1-01 using ImageJ. Green, blue, and red represent amphiboles, opaque minerals, and plagioclase, respectively. Areas with a combination of colors represent conflicts.

### 4.1.3. Point Counting Using ImageJ

The point count took 30 minutes to go over 336 points and measure the major axis of crystals in each class. The result was 108 measurements of the major axis. Extrapolated to measurements of minor and major axes (to create ellipses) for ten samples this would require about ten hours of work.

### 4.1.4. Manual Segmentation

To manually trace the outlines of objects in one quarter of sample GD-T1-01, took 40 minutes. Resulting in a total of 627 outlines (see Figure 4.2). Extrapolating to fully outlines minerals in ten samples comes to more than 25 hours of work.

| Method | Work Time for 10 Samples |
|---|---|
| arivis Cloud (1500 annotations) | 4-5 hours |
| Intensity Based ImageJ | 20 hours |
| Point Counting | 10 hours |
| Manual Outlining | 25+ hours |

**Table 4.2:** Time taken for different methods of data collection and segmentation.



**Figure 4.2:** Manual segmentation of GD-T1-01 using Goodnotes on an iPad. Green, blue, and red are amphiboles, opaque minerals, and plagioclase respectively.

## 4.2. Output Data From Python

This section displays examples of figures created in this project which were used to compare models. In addition, these figures can be used for geologic interpretation. Figure 4.3 is an example of a segmentation created using arivis Cloud. Figure 4.4 is the same segmentation with each crystal reduced to their major axis, illustrating their orientation across the sample. Some major axes align with the intuitive major axis, while others do not. The empty space seen in these figures are areas which contain large plagioclase crystals which have not been identified by the model.

Figures 4.5 and 4.6 illustrate the distribution of orientation and crystal size between classes for one sample. Comparison of these figures across the Sosa Dyke provides information of textural variability across the dyke. Please note arivis considers 0 degrees to be at the three o'clock position. As an example, Figure 4.7 plots the variability of two measurements within one figure. The digital appendix contains the full plots for each model created.

In appendices B and C the segmentation and associated figures can be found for Bright25-bestv2 and CPl25-bestv2 models. The digital appendix contains all segmentations, major axis plots, rose plots and CSDs for each model created.

Data from the bright25-best model shows mean area generally increasing towards the center of the dyke. The trend is most consistent among amphiboles. Orientation shows groupings of classes together, but there is no clear trend across the dyke.
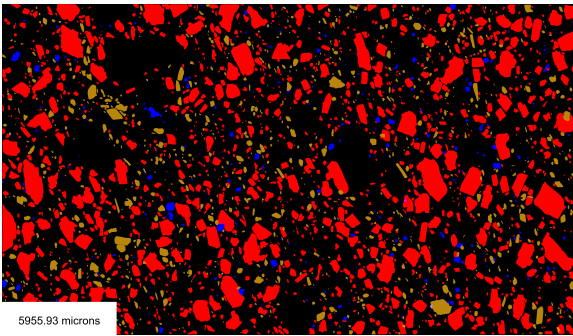


**Figure 4.3:** Segmentation of GD-T1-01 using the Bright25-bestv2 model. Dark goldenrod, blue, and red are amphiboles, opaque minerals, and plagioclase respectively.
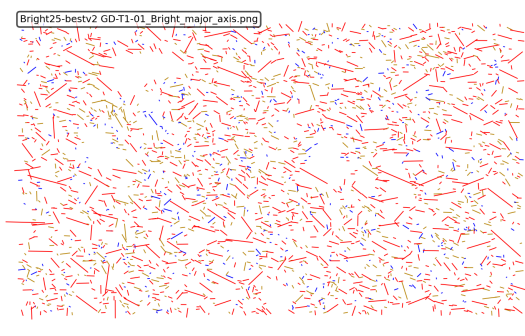


**Figure 4.4:** Major axis plot of GD-T1-01 using the Bright25-bestv2 model. Dark goldenrod, blue, and red are amphiboles, opaque minerals, and plagioclase respectively.
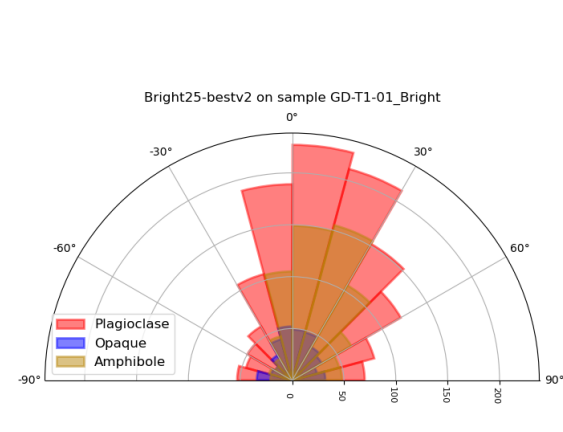
**Figure 4.5:** Rose plot displaying orientations of crystals in GD-T1-01 segmented using the Bright25-bestv2 model. 0 degrees is at the three o'clock position of the sample.
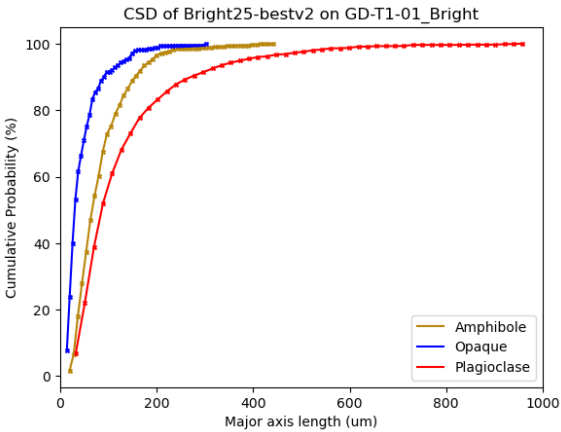


**Figure 4.6:** Crystal size distribution (CSD) of sample GD-T1-01 segmented using the Bright25-bestv2 model. Note xlim is set manually for this example image. For images found in appendix B and C xlim is set automatically to the largest crystal size in the entire dataset for comparison between samples.
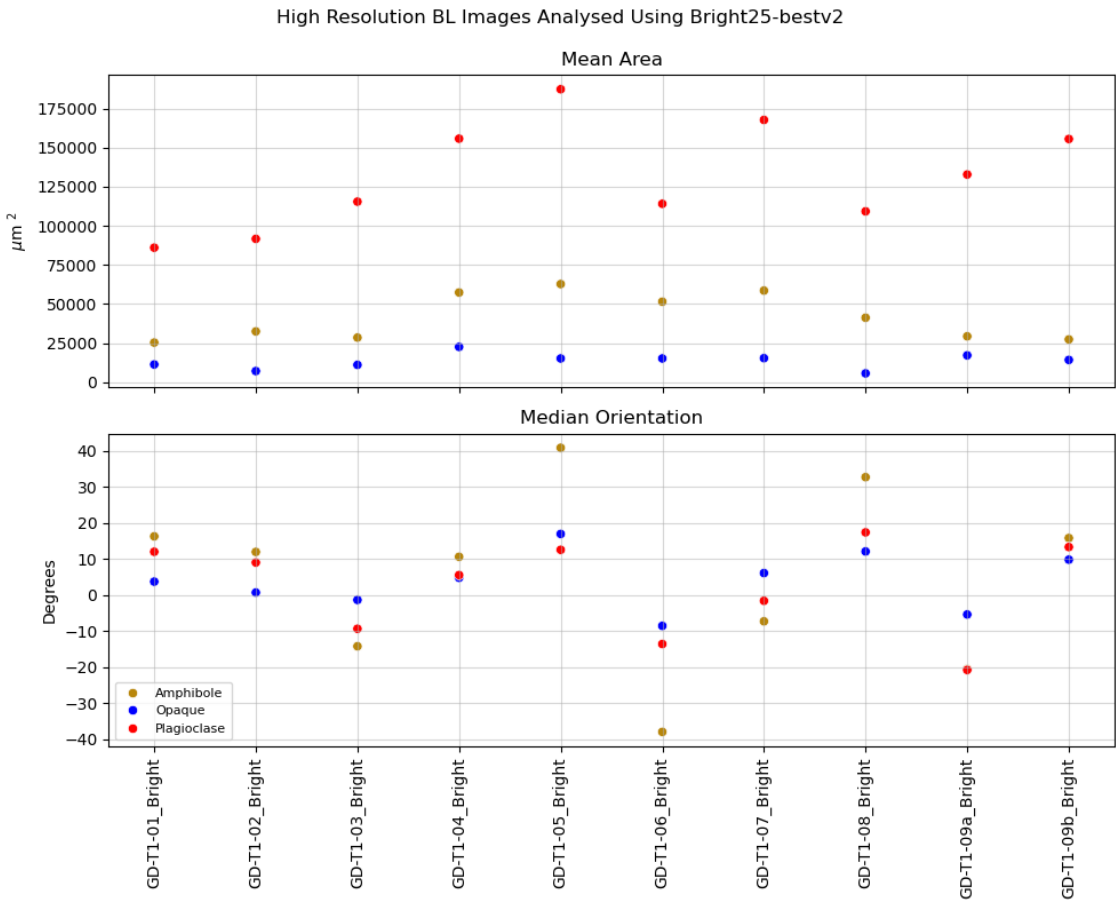


**Figure 4.7:** Some examples of data plotted per class across the Sosa dyke which can be used for geologic interpretation. Data is from high resolution images segmented using the Bright25-bestv2 model.

# 4.3. Number of Annotations

For models T1-01-bright10 up to iteration T1-01-bright10v4, Figure 4.8 shows increasing the amount of annotations of plagioclase crystals had an impact on both the number of plagioclase predictions made, as well as the

percentage of the total area which the model identifies as plagioclase. Initially, the number of predictions increases rapidly, coupled with an increase of percent area. However, as more annotations are made, both indicators seem to settle at an asymptote.

On images GD-T1-09a and GD-T1-09b (segmentations can be found in the digital appendix), the T1-01-bright10v4 did sometimes segment areas with blue dye as plagioclase. Although many of the areas with blue dye were not falsely segmented, using the background class to exclude those pixels from the training data would eliminate this inaccuracy.
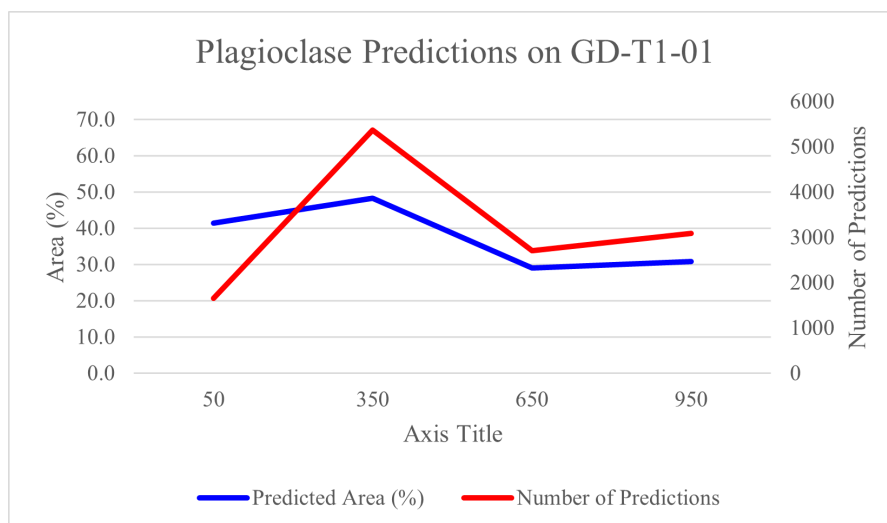


**Figure 4.8:** The number of plagioclase predictions and total area predicted as plagioclase plotted against the number of annotations made.

## 4.4. Resolution

The CPL25_v1 is inconsistent with the other three models created in this section. Figure 4.9 shows that for samples analyzed, GD-T1-01 is found to have the most objects, followed by GD-T1-05 and GD-T1-09a on all three models except CPL25_v1. Across both image types, higher resolution images find more crystals in the analyzed samples (Figure 4.10). In BL images, while there is a 26% increase in number of objects identified in high resolution images, there is a 19% decrease in sample area segmented (Table 4.3). More predictions but less area is indicative of objects which are smaller. As an example, the mean crystal area of amphiboles (as a fraction of total sample area) are $5.0 \cdot 10^{-5}$ for the low resolution bright image and $1.8 \cdot 10^{-5}$ for the high resolution image.

Figure 4.11 shows a decrease in area segmented for all classes under BL. Under CPL the area segmented as amphiboles and plagioclase also decrease, but the area of opaque minerals increases enough to reach a net 0% increase in area.
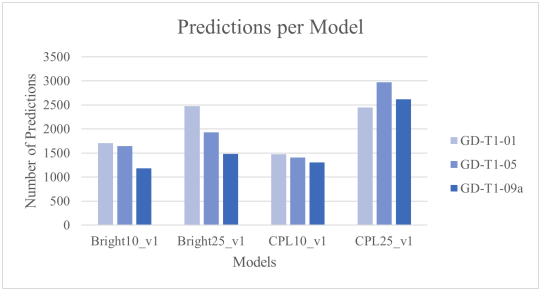
**Figure 4.9:** The total number of crystals found by models with different resolutions on samples GD-T1-01, GD-T1-05, GD-T1-09a.
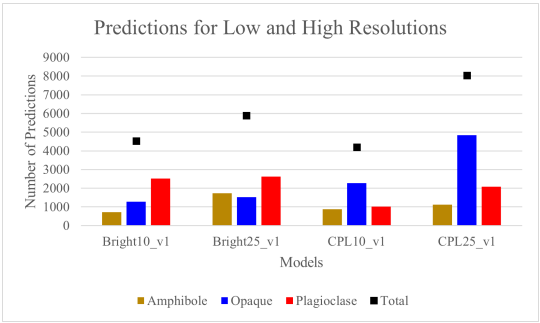


**Figure 4.10:** The total number of crystals found for each different class (amphiboles, opaque, and plagioclase) by models with different resolutions on samples GD-T1-01, GD-T1-05, GD-T1-09a.
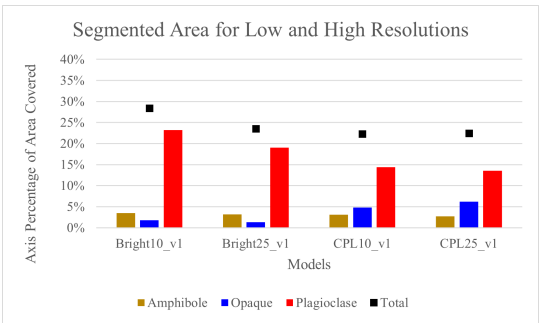


**Figure 4.11:** Percentage of the area covered by each class for bright and CPL models with low and high resolutions on samples GD-T1-01, GD-T1-05, and GD-T1-09a.

| Class | Bright | CPL |
|---|---|---|
| | **Count** | |
| Amphibole | 82% | 24% |
| Opaque | 17% | 72% |
| Plagioclase | 4% | 78% |
| **Total Increase by Count** | 26% | 63% |
| | **Area** | |
| Amphibole | -10% | -15% |
| Opaque | -28% | 26% |
| Plagioclase | -20% | -6% |
| **Total Increase by Area** | -19% | 0% |

**Table 4.3:** The percent difference between the number of crystals found in low and high resolution images for each class. Positive values indicate more objects found in higher resolution images.

## 4.5. Bright&CPL

Figure 4.12 shows a significantly less crystals identified on high resolution images compared to low resolution. On CPL images, a larger number and greater area the of the image is segmented as opaque minerals (Figures 4.12 and 4.14). Figure 4.14 shows a larger portion of the sample area is segmented as plagioclase on BL images than CPL.

For both image types, the area segmented as plagioclase increases throughout the iterative process. The number of predicted amphiboles stays relatively consistent throughout, which is also seen in the total segmented area which varies from 2.5 to 4%. This is in contrast to opaque minerals which varies more both in number segmented as well as area, with a range of 1.7-5.9%.
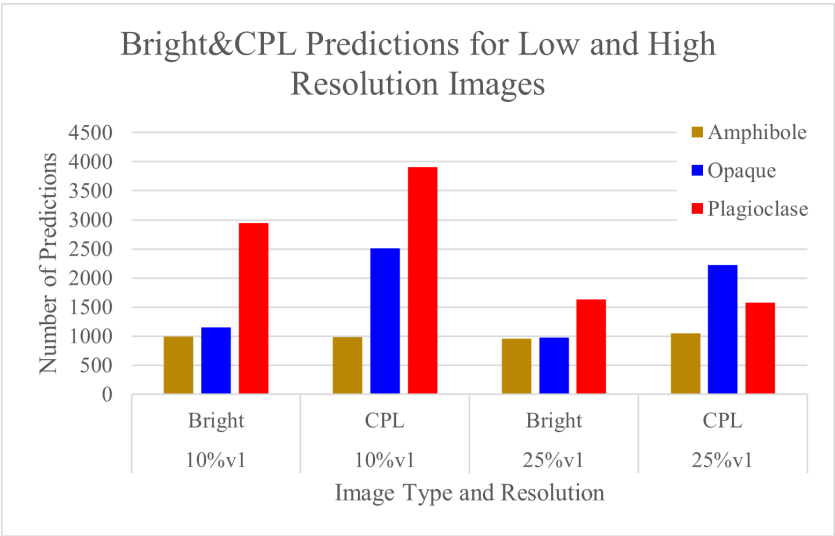
**Figure 4.12:** The number of crystals found on samples GD-T1-01, GD-T1-05, and GD-T1-09a by low and high resolution Bright&CPL models.
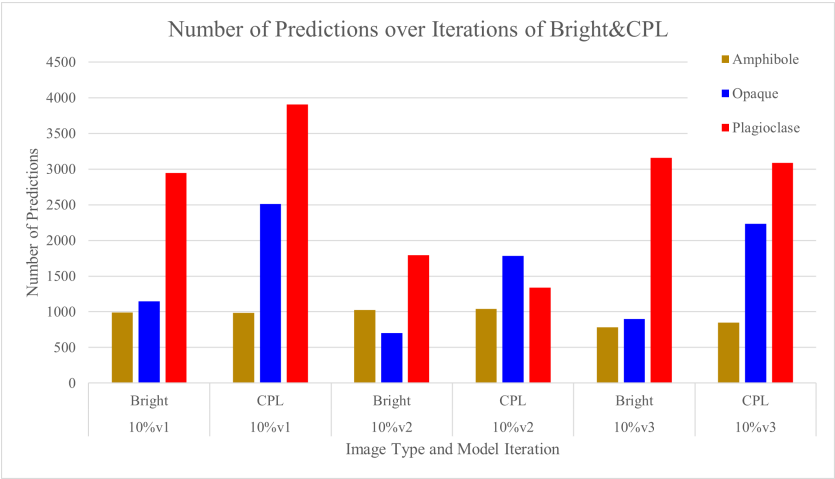


**Figure 4.13:** The number of crystals found on samples GD-T1-01, GD-T1-05, and GD-T1-09a by multiple iterations of low resolution Bright&CPL models.
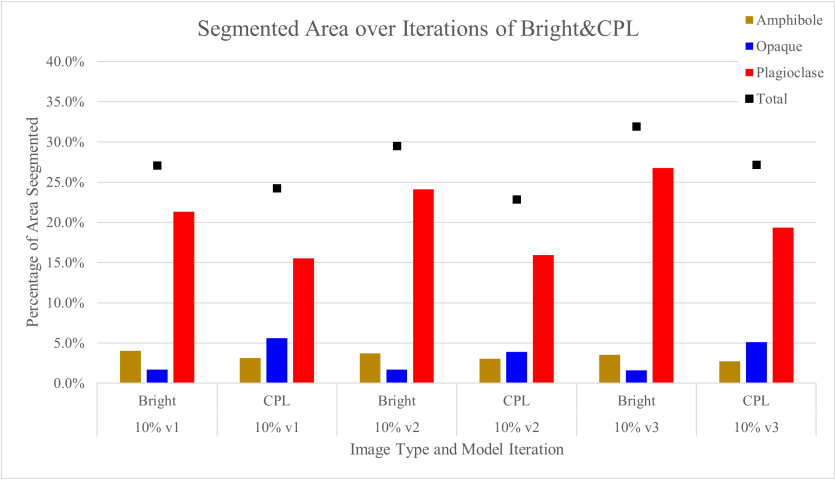


**Figure 4.14:** Percentage of the total sample area segmented by iterations of the low resolution Bright&CPL models for samples GD-T1-01, GD-T1-05, and GD-T1-09a.

# 4.6. High Resolution, Many Annotations

The Bright25-bestv2 and CPL25-bestv2 were created to determine what can be done if a significant amount of time (see table 4.2) is spent to annotate samples on high resolution images. An example of the resulting segmentation is shown in Figure 4.15. The rest of these segmentations can be found in appendices B and C.

There are significant differences between the BL and CPL model. As shown in Tables 4.4 and 4.5, overall the model trained on BL images segments a greater are of the image as crystals. The CPL model identifies more opaque minerals and segments a greater area.

Figure 4.16 shows the range for major axis length is far greater for plagioclase than amphiboles or opaque minerals. All models display a similar trend. Those figures can be found in the digital appendix.

Figure 4.17 displays the distribution of eccentricity per class for the BL model. Amphiboles and plagioclase are more eccentric and show an downward skewed distribution. Opaque minerals display a more uniform distribution at a lower eccentricity.

| Class | Bright25-bestv2 | CPL25-bestv2 |
|---|---|---|
| Amphibole | 3% | 3% |
| **Count** | 5368 | 4148 |
| Opaque | 1% | 3% |
| **Count** | 6380 | 9321 |
| Plagioclase | 20% | 13% |
| **Count** | 10955 | 7107 |

**Table 4.4:** Across all ten samples, the number of objects found for each class as well as the percentage of the total area.

| Sample | BL | CPL |
|---|---|---|
| GD-T1-01 | 28% | 24% |
| GD-T1-02 | 25% | 18% |
| GD-T1-03 | 28% | 23% |
| GD-T1-04 | 24% | 11% |
| GD-T1-05 | 29% | 19% |
| GD-T1-06 | 22% | 12% |
| GD-T1-07 | 25% | 15% |
| GD-T1-08 | 29% | 27% |
| GD-T1-09a | 25% | 24% |
| GD-T1-09b | 30% | 23% |

**Table 4.5:** Percentage of the total area segmented as amphibole, opaque or plagioclase.
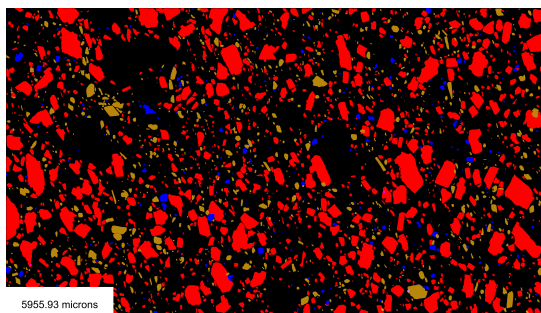


**Figure 4.15:** Segmentation of GD-T1-01 using the Bright25-bestv2 model. Dark goldenrod, blue, and red are amphiboles, opaque minerals, and plagioclase respectively.
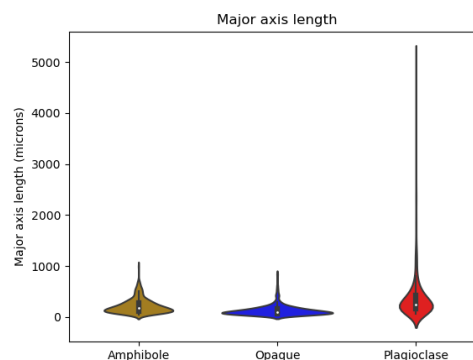


**Figure 4.16:** Distribution of major axis length for all samples when segmented using model Bright25-bestv2.
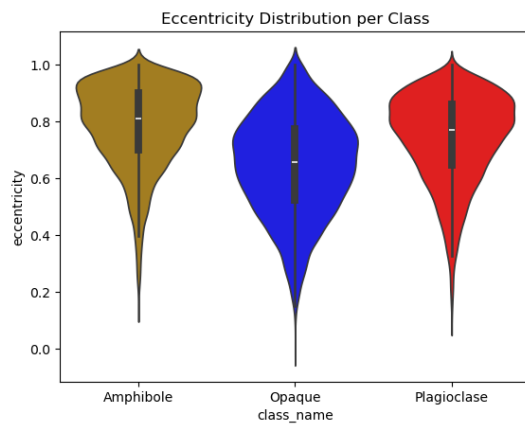
**Figure 4.17:** Eccentricity of each class when high-resolution sample images are segmented with model Bright25best-v2

# 5

# Discussion

As shown in Figure 4.8, after about 700 annotations (1.5-3 hours of work) the area segmented on one sample reaches a plateau. This suggests the model has identified most plagioclase crystals on the section, which is corroborated by inspection of the segmentation. Studies investigating the effects of the number of annotations on accuracy, find a similar plateau [3, 24]. Although arivis Cloud does not provide an explicit accuracy score, inspection of the segmented image allows the user to identify when this plateau has been reached. The number of annotations required to reach this plateau depends on the difficulty of segmentation and variation between images.

One source of variation in this project are samples GD-T1-09a and GD-T1-09b which were prepared using a blue dye instead of only clear epoxy. More annotations were required to deal with this variation. To create a robust model across different samples, research on object-based segmentation indicates that, more training data leads to better model performance [1]. However, at a point, the plateau is reached and increasing the number of annotations is no longer paired with substantial increases in accuracy. Annotation is time-consuming. To decrease the amount of time spent annotating, arivis Cloud recommends standardizing the method of thin section preparation and scanning.

In this project it is shown that the annotation person-hours required to create the segmentation of ten samples using arivis Cloud (5 hours) is significantly less than intensity-based segmentation (20 hours), point counting (10 hours), and manual outlining (25 hours). Other studies are in agreement that traditional methods are time-consuming and attempt to decrease this by using machine learning to increase the efficiency of intensity-based segmentation and point counting [5, 25]. One of the strengths of arivis Cloud, is that when a model has been and achieves sufficient accuracy, it can be applied to an entire dataset. As dataset size increases, time savings become more substantial. However, the cloud-based computation time does increase, but this can be scheduled to be run outside of working hours.

Figures 4.4, 4.5 and 4.6 were created using some of the many measurements which arivis Cloud performs on each identified crystal. The full list of measurements which it performs can be found in appendix A. This data can be plotted across the dyke and provide new geologic insights and allows for corroboration with current geologic knowledge. While the data is incredibly useful, there are still limitations. For example, in major axis plots (ex. Figure 4.4), the major axis does not always align with the intuitive major axis. It is unclear whether this originated from the analysis code or an inherent limitation of arivis Cloud's measurement algorithm. Despite such issues, the combination of increased time efficiency and vast data output, makes AI-based segmentation a powerful tool for petrographic analysis, providing opportunities for new geologic insights.

Higher resolution models are less consistent in identifying large (plagioclase) crystals than lower resolution models. This decrease in segmented area is shown in Figure 4.11 and Table 4.3. Inspection of high resolution models further confirms this result. The percentage of total area segmented per sample as listed in Table 4.5 can be interpreted as crystal content values. However, when compared to crystal content values from Schmiedel et al. (2021) as seen in Table 5.1, the arivis models identify significantly fewer crystals. An investigation into the segmentation of sample GD-T1-01 using the Bright25-bestv2 (a high resolution model) revealed that undetected large plagioclase crystals account for approximately 4% of the total sample area. One possible factor contributing to this inconsistency is an annotation bias, specifically, the tendency to annotate smaller crystals. As illustrated in Figure 4.16, for plagioclase, the vast majority of crystals are small. When annotating a representative dataset, users naturally select a higher number of smaller crystals as they are more abundant. In addition, since large crystals occupy a disproportionate amount of the total sample area, annotating only a few may seem to make their representation sufficient. As a result, users may further prioritize annotating smaller crystals, leading to a dataset skewed towards larger objects. Since the AI model learns from the annotated dataset, this bias likely reduces segmentation accuracy for larger crystals [11]. Accounting for as much variability within a class is essential for creating an accurate model [9]. Creating separate classes for 'small' and 'large' plagioclase crystals could be an option, however this could lead to many classification conflicts between the two classes. Another, and perhaps the

most compelling explanation for the model's difficulty in segmenting large plagioclase crystals, is that according to arivis Cloud documentation, "for optimal results, object sizes should be no larger than 320*320 pixels" [11]. This constraint is more prominent in high resolution image, where objects of larger pixel areas are inherently more common. For example, in the BL resolution test, the low resolution model identified 11 occurrences of objects larger than 320*320 pixels compared to 111 occurrences found by the high resolution model. This limits both the range of crystal sizes which can be segmented and the maximum resolution which can be used to create an arivis Cloud model.

While higher resolution images contain finer details, their effectiveness is limited when segmenting large objects, potentially due to annotation bias or constraints within the arivis Cloud algorithms. Although high resolution models less consistently identify large plagioclase crystals, they make fewer mistakes distinguishing between opaque minerals and amphiboles than low resolution models, based on inspection and comparison. Figure 5.1 shows some of these mistakes. Research on geographic object based image analysis for land cover classification finds similar effects, stating that "a large segmentation scale cannot precisely extract relatively small objects" [12]. The same study concludes that "segmentation scales are strongly correlated with an object's average area" [12]. Selecting the appropriate resolution is crucial for model accuracy as this is crucial for classification accuracy [10, 16]. Potential methods for the optimization of resolution for segmentation accuracy include trial-and-error based methods, statistical methods and the combination of multiple scale factors [18, 28]. The most applicable to arivis Cloud are trial-and-error, and potentially the combination of resolutions and/or methods. For example, since amphiboles and opaque minerals have a similar size distribution and are relatively small, a high resolution model would be optimal. This could be combined with a lower resolution model for plagioclase or even an intensity-based segmentation of plagioclase. To conclude, optimizing resolution based on object size and size distribution is a crucial step for improving model accuracy in arivis Cloud.

| Sample | BL | CPL | Schmiedel et al. (2021) |
|--------|------|-------|-------------------------|
| GD-T1-01 | 28% | 24% | 36.9% |
| GD-T1-02 | 25% | 18% | 35.0% |
| GD-T1-05 | 29% | 19% | 35.5% |
| GD-T1-09 | 27.5% | 23.5% | 37.5% |

**Table 5.1:** Comparison between crystal content found by models Bright25-bestv2, CPL25-bestv2 and data from Schmiedel et al. (2021). In Schmiedel et al. (2021) there was no distinction made between samples GD-T1-09a and GD-T1-09b. For comparison, the average was taken between samples GD-T1-09a and GD-T1-09b. Full results can be found in Table 4.5

Based on observation, the models trained and used on CPL images were less accurate than those trained on BL based on observation of the segmented images. This is due to the variability in degree of extinction within a single crystal. For plagioclase crystals, zones in extinction were often segmented as opaque minerals or amphiboles. In addition, zones under different extinction phases are often segmented as separate crystals. Due to these inaccuracies, models trained on BL images yielded better results in this project.

Combining BL and CPL images into a single dataset and training a model based on annotations from both images types resulted in a total segmented area of 32% when applied to BL images, which is closer to the crystal content values from Schmiedel et al. (2021) than other models created in this project. Figure 5.2 shows that while the model performs reasonably well on BL images, it severely under-performs when applied to CPL images. The combination of image types potentially allows the model to gather more information on the internal features through the CPL images, which can help in distinguishing between features not or barely visible under BL. Although the combination of images under different types of light goes against the recommendations of the arivis Cloud documentation, this might be incredibly useful method to distinguish crystals which appear similar under BL, but contain different features visible under CPL. A downside however, is that annotating both BL and CPL images required double the annotation effort. Applying the same annotation effort to only BL images might prove to be more accurate. Future work could further investigate this method.
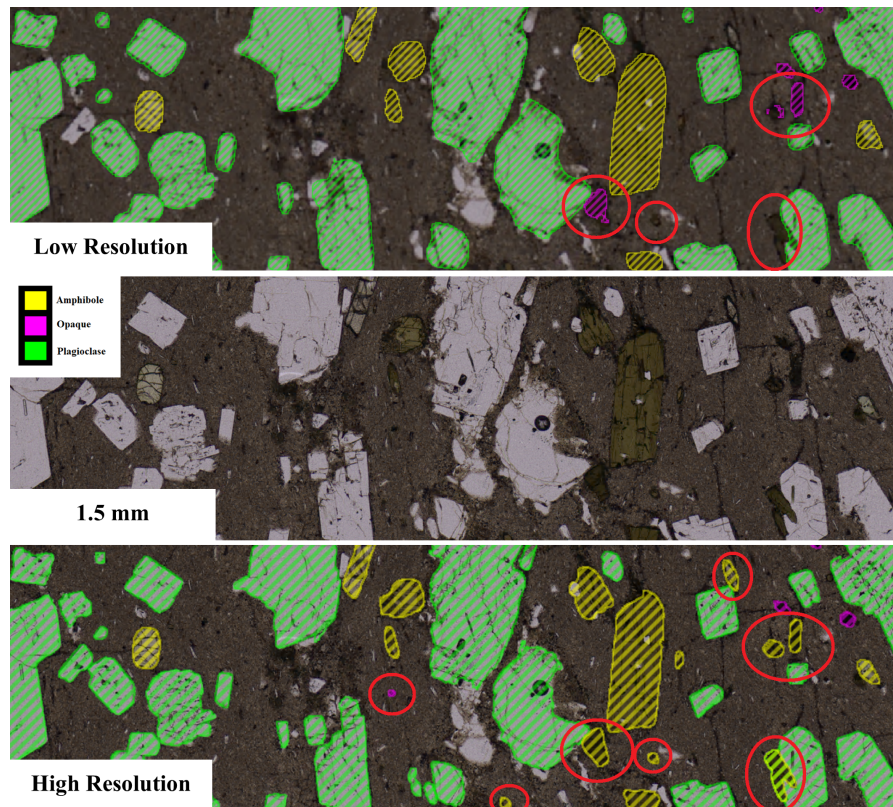
**Figure 5.1:** Observed differences for opaque minerals and amphiboles on a small portion of GD-T1-01 under BL when segmented using low and high resolution models. Differences are marked in red.
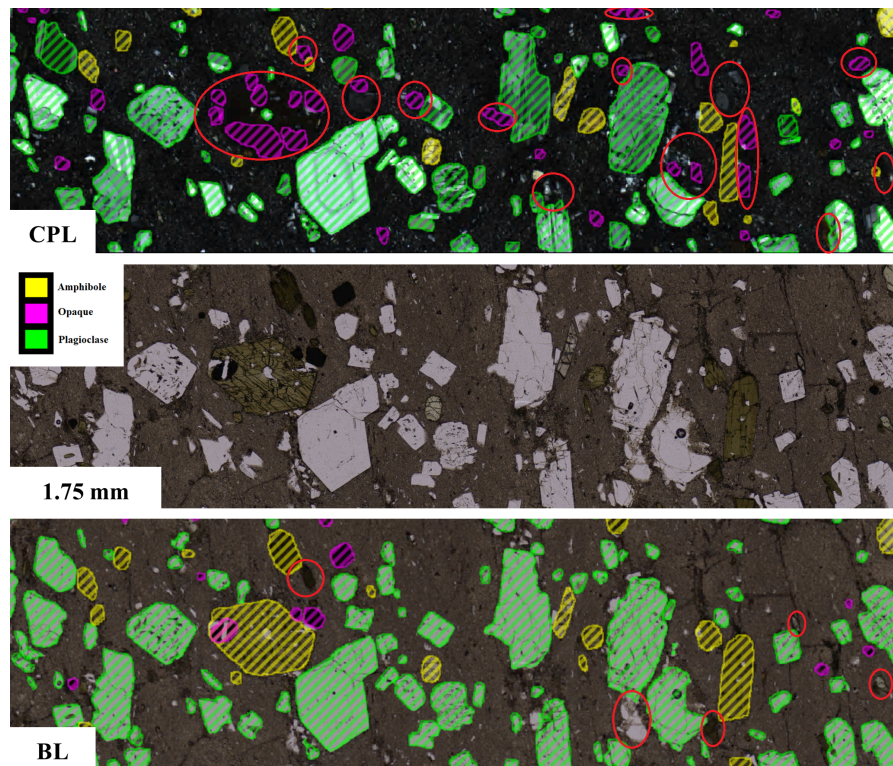


**Figure 5.2:** Some observed inaccuracies on a small portion of GD-T1-01 when the model bright&CPL 10% v3 is used to segment BL and CPL images. Inaccuracies are marked in red.

In Figure 4.7 plagioclase exhibits the largest difference in mean crystal area between the margin of the dyke and the center. The trend is most clearly visible for samples GD-T1-01 to GD-T1-05. However, as mentioned in previous sections, high resolution models tend to under segment large plagioclase crystals which could be an explanation for this inconsistency. Opaque minerals do not show a clear spatial trend, likely due to their small size, limiting visibility on the figure. Amphiboles, which are generally segmented with higher accuracy, do show a consistent trend of increasing area towards the center of the dyke. Literature on mafic dykes find a similar trend, expecting larger crystals in the center of the dyke than in the margin [2, 19]. The size difference could be explained by the larger temperature differential at the margin, leading to more rapid cooling than at the center [15, 19]. Alternatively research on the rheology of high viscosity magmas indicate shear thinning or shear thickening could be the cause of crystal size reduction or brecciation at the conduit margin [21, 22]. The observed crystal size reduction at the Sosa Dyke aligns with current geologic understanding, supporting arivis Cloud's applicability to geologic research.

Figure 4.17 shows that opaque minerals are more uniformly distributed at a lower eccentricity whereas amphiboles and plagioclase display higher eccentricities. In a thin section, mineral grains are randomly cut. Elongate crystals are likely to display a more eccentric cross section than less elongate minerals. This observation aligns with mineralogical knowledge as amphiboles and plagioclase have a more elongate shape compared to the opaque minerals which are more isometric in shape [17]. Since the elongate minerals appear more eccentric in a thin section, their measured orientation is more indicative of orientation than that of more spherical crystals. Among these amphiboles are segmented more accurately and consistently, and therefore likely a more reliable indication of orientation than plagioclase. That said, there is no clear orientation trend visible across the dyke as the orientation of the thin sections was not recorded during sampling. As a result, the orientation of the crystals is in reference to the thin section rather than the dyke. However, if the thin sections had been oriented, the crystal orientations could potentially be used to determine the magma flow history within the dyke [2, 26].

Some samples contained plagioclase crystals with weathered areas. These areas are consequently filled with epoxy during preparation of the thin sections. In BL images, these crystals no longer display the internal features characteristic of plagioclase. Under CPL, the epoxy-filled areas are under complete extinction. Since opaque minerals are also under complete extinction, the model likely falsely classifies epoxy filled plagioclase as opaque minerals.

The samples used in this project were trachyte/trachydacite in composition [23]. Due to the nature of these rocks, small amount of quartz can be expected [4]. However, distinguishing between small plagioclase crystals and quartz was difficult in low resolution images. Since no separate class for quartz was created, some of the plagioclase is falsely classified.

ZEISS software such as ZEN and ZEN core is typically required to segment the output data following the standard ZEISS arivis Cloud procedure as seen in Figure 3.2 [11]. In this project I did not have access to these software and instead developed a Python script to create the final segmented image and analyze the data. This code is included in the digital appendix.

While arivis Cloud is a powerful tool, it presents several limitations in usability and application. Many models were created to investigate the effects of number of annotations, resolution, image type and combining BL and CPL images. Due to the constraint of computation time and the project deadline, a limited number of iterations were made for each model. More iterations could yield different results [8]. There was also the issue of reproducibility of the annotations. Each new model required re-annotating from scratch. In this project, the scanned portions of a sample under BL and CPL images are exactly the same. Creating an annotation layer for one sample and applying to all versions of the image would be incredibly useful. This would reduce the time spent annotating and improve the reliability of the results of this project as there would be no variation in annotations across models. This would also improve the accuracy of certain annotations, as some crystals are easier to differentiate under BL and some under CPL. Finally, the arivis Cloud software displays an automatically generated scale bar in the image. However, for all images used in this project the scale bar was overestimated by several orders of magnitude. The source of this error could possibly lie within the image metadata, the platform itself, or elsewhere. Arivis Cloud uses this scale bar to convert pixels to $\mu$m in the measurement.csv output file leading to incorrect measurements. This error is adjusted for within the Python code.

<div align="right">

**6**

# Conclusion

</div>

The aim of this project was to determine to what extent object-based segmentation using ZEISS arivis Cloud can be used to segment similar mineral phases with different textural parameters in petrographic thin sections. This was done by creating models within arivis Cloud to investigate the effects of annotation, image resolution and image type (BL or CPL) on the resulting segmentation. The thin sections used in this study were taken from the Sosa Dyke in Argentina by the authors of Schmiedel et al. (2021).

The following conclusions could be made:

1. ZEISS arivis Cloud can be used to segment petrographic thin sections using object-based AI models.

2. Models trained on BL images predict percentage of total area segmented closer to crystal content values of Schmiedel et al. (2021) than models trained on CPL images. CPL models often misclassify areas of complete extinction in plagioclase crystals as opaque minerals.

3. Models trained with more annotations across diverse samples segment a larger percentage of total sample area, suggesting that increased annotations improve accuracy.

4. Models trained on high resolution images were less consistent in predicting large (plagioclase) crystals than models trained on low resolutions. This could be due to annotation bias towards smaller crystals or because arivis Cloud may not perform optimally when objects are larger than 320*320 pixels [11]. However, higher resolutions were more accurate at distinguishing between opaque minerals and amphiboles on BL images.

5. Combining annotations on images of samples under BL and CPL into one model may improve segmentation of BL images. However, this approach contradicts recommendations from the arivis Cloud documentation and requires further study.

6. ZEISS arivis Cloud's Object-based segmentation can significantly reduce time compared to other manual and intensity based segmentation methods. For the ten samples in this project, manual methods took at least twice as long. The time savings increase with larger datasets of similar thin sections. In addition, ZEISS arivis Cloud produces data (eg. major axis length, orientation, area, eccentricity etc.) which can be used for geologic interpretation.

This study demonstrates that ZEISS arivis Cloud can effectively segment petrographic thin sections. While challenges such as annotation bias and inconsistent segmentation of large crystals remain, the platform has the potential to significantly reduce the time required for petrographic analysis compared to manual and intensity-based segmentation methods. With further optimization, the platform could become an important tool used to analyze thin sections, which were previously deemed too time consuming, potentially unlocking new geologic insights. Future research should focus on annotation strategies, improving model accuracy and investigate the applicability across different rock types.

# References

[1]  Cathaoir Agnew et al. "Annotation Quality Versus Quantity for Object Detection and Instance Segmentation". In: *IEEE Access* 12 (2024), pp. 140958–140977. DOI: 10.1109/ACCESS.2024.3467008.

[2]  Ceri Allgood. "Interpreting dyke propagation and emplacement dynamics using crystal and vesicle textures". Available at Durham E-Theses Online. PhD thesis. Durham University, 2024. URL: http://etheses.dur.ac.uk/15689/.

[3]  Bjorn Barz and Joachim Denzler. "Deep learning on small datasets without pre-training using cosine loss". In: *Proceedings of the IEEE/CVF winter conference on applications of computer vision*. 2020, pp. 1371–1380.

[4]  R. Bonewitz. *Rocks and Minerals*. DK nature guide. DK Publishing, 2012. ISBN: 9781405375863. URL: https://books.google.nl/books?id=S1OMtgAACAAJ.

[5]  Semen Budennyy et al. "Image Processing and Machine Learning Approaches for Petrographic Thin Section Analysis (Russian)". In: Jan. 2017. DOI: 10.2118/187885-RU.

[6]  Steffi Burchardt. "Chapter 1 - Introduction to Volcanic and Igneous Plumbing Systems—Developing a Discipline and Common Concepts". In: *Volcanic and Igneous Plumbing Systems*. Ed. by Steffi Burchardt. Elsevier, 2018, pp. 1–12. ISBN: 978-0-12-809749-6. DOI: https://doi.org/10.1016/B978-0-12-809749-6.00001-7. URL: https://www.sciencedirect.com/science/article/pii/B9780128097496000017.

[7]  Steffi Burchardt et al. "Progressive Growth of the Cerro Bayo Cryptodome, Chachahuén Volcano, Argentina—Implications for Viscous Magma Emplacement". In: *Journal of Geophysical Research: Solid Earth* 124.8 (2019), pp. 7934–7961. DOI: https://doi.org/10.1029/2019JB017543. eprint: https://agupubs.onlinelibrary.wiley.com/doi/pdf/10.1029/2019JB017543. URL: https://agupubs.onlinelibrary.wiley.com/doi/abs/10.1029/2019JB017543.

[8]  Carl Zeiss Microscopy GmbH. *arivis Cloud*. Munich, Germany, 2024. URL: https://www.apeer.com.

[9]  Lucas von Chamier, Romain F Laine, and Ricardo Henriques. "Artificial intelligence for microscopy: what you should know". In: *Biochemical Society Transactions* 47.4 (2019), pp. 1029–1040.

[10]  Lucian Drăguţ et al. "Automated parameterisation for multi-scale image segmentation on multiple layers". In: *ISPRS Journal of photogrammetry and Remote Sensing* 88 (2014), pp. 119–127.

[11]  Carl Zeiss Microscopy GmbH. *arivis Cloud docs*. 2024. URL: https://docs.arivis.cloud/.

[12]  Shuang Hao, Yuhuan Cui, and Jie Wang. "Segmentation Scale Effect Analysis in the Object-Oriented Method of High-Spatial-Resolution Image Classification". In: *Sensors* 21.23 (2021). ISSN: 1424-8220. DOI: 10.3390/s21237935. URL: https://www.mdpi.com/1424-8220/21/23/7935.

[13]  E Herrero-Bervera et al. "Magnetic fabric and inferred flow direction of dikes, conesheets and sill swarms, Isle of Skye, Scotland". In: *Journal of Volcanology and Geothermal Research* 106.3 (2001), pp. 195–210. ISSN: 0377-0273. DOI: https://doi.org/10.1016/S0377-0273(00)00293-6. URL: https://www.sciencedirect.com/science/article/pii/S0377027300002936.

[14]  N. Jim. "Fracture characterization in magmatic rock, a case study of the Sosa-dyke (Neuquén Basin, Argentina)". Dissertation. Uppsala University, 2020. URL: https://urn.kb.se/resolve?urn=urn:nbn:se:uu:diva-411548.

[15]  Janine L. Kavanagh. "Chapter 3 - Mechanisms of Magma Transport in the Upper Crust—Dyking". In: *Volcanic and Igneous Plumbing Systems*. Ed. by Steffi Burchardt. Elsevier, 2018, pp. 55–88. ISBN: 978-0-12-809749-6. DOI: https://doi.org/10.1016/B978-0-12-809749-6.00003-0. URL: https://www.sciencedirect.com/science/article/pii/B9780128097496000030.

[16]  Minho Kim et al. "Multi-scale GEOBIA with very high spatial resolution digital aerial imagery: scale, texture and image objects". In: *International Journal of Remote Sensing* 32.10 (2011), pp. 2825–2850. DOI: 10.1080/01431161003745608.

[17] Cornelis Klein and Anthony Philpotts. *Earth materials 2nd edition: Introduction to mineralogy and petrology*. 2nd ed. Cambridge, England: Cambridge University Press, 2016. ISBN: 9781316608852.

[18] Jianhua Liu, Mingyi Du, and Zhengyuan Mao and. "Scale computation on high spatial resolution remotely sensed imagery multi-scale segmentation". In: *International Journal of Remote Sensing* 38.18 (2017), pp. 5186–5214. DOI: 10.1080/01431161.2017.1325536.

[19] E. Donald Ngonge, C.J. Archanjo, and M.H.B.M. Hollanda. "Plagioclase crystal size distribution in some tholeiitic mafic dykes in Cabo Frio–Buzios, Rio de Janeiro, Brazil". In: *Journal of Volcanology and Geothermal Research* 255 (2013), pp. 26–42. ISSN: 0377-0273. DOI: https://doi.org/10.1016/j.jvolgeores.2013.01.009. URL: https://www.sciencedirect.com/science/article/pii/S0377027313000279.

[20] J. Octavio Palma et al. "Stratigraphy and structure of Chachahuén volcanic complex, southern Mendoza province, Argentina". In: *Journal of South American Earth Sciences* 140 (2024), p. 104900. ISSN: 0895-9811. DOI: https://doi.org/10.1016/j.jsames.2024.104900. URL: https://www.sciencedirect.com/science/article/pii/S0895981124001226.

[21] Mattia Pistone et al. "Deformation experiments of bubble- and crystal-bearing magmas: Rheological and microstructural analysis". In: *Journal of Geophysical Research: Solid Earth* 117.B5 (2012). DOI: https://doi.org/10.1029/2011JB008986. eprint: https://agupubs.onlinelibrary.wiley.com/doi/pdf/10.1029/2011JB008986. URL: https://agupubs.onlinelibrary.wiley.com/doi/abs/10.1029/2011JB008986.

[22] Mattia Pistone et al. "Rheological flow laws for multiphase magmas: An empirical approach". In: *Journal of Volcanology and Geothermal Research* 321 (2016), pp. 158–170.

[23] Tobias Schmiedel et al. "Emplacement and Segment Geometry of Large, High-Viscosity Magmatic Sheets". In: *Minerals* 11.10 (2021). ISSN: 2075-163X. DOI: 10.3390/min11101113. URL: https://www.mdpi.com/2075-163X/11/10/1113.

[24] Saleh Shahinfar, Paul Meek, and Greg Falzon. ""How many images do I need?" Understanding how sample size per class affects deep learning model performance metrics for balanced designs in autonomous wildlife monitoring". In: *Ecological Informatics* 57 (2020), p. 101085.

[25] David G. Tang, Kitty L. Milliken, and Kyle T. Spikes. "Machine learning for point counting and segmentation of arenite in thin section". In: *Marine and Petroleum Geology* 120 (2020), p. 104518. ISSN: 0264-8172. DOI: https://doi.org/10.1016/j.marpetgeo.2020.104518. URL: https://www.sciencedirect.com/science/article/pii/S0264817220303019.

[26] Rémi Vachon et al. "Crystal rotations and alignment in spatially varying magma flows: 2-D examples of common subvolcanic flow geometries". In: *Geophysical Journal International* 226.1 (Mar. 2021), pp. 709–727. ISSN: 0956-540X. DOI: 10.1093/gji/ggab127. eprint: https://academic.oup.com/gji/article-pdf/226/1/709/42162340/ggab127.pdf. URL: https://doi.org/10.1093/gji/ggab127.

[27] Ian K. Whitbread. "Petrography". In: *Encyclopedia of Geoarchaeology*. Ed. by Allan S. Gilbert et al. Cham: Springer International Publishing, 2020, pp. 1–5. ISBN: 978-3-030-44600-0. DOI: 10.1007/978-3-030-44600-0_23-1. URL: https://doi.org/10.1007/978-3-030-44600-0_23-1.

[28] Badia Ez-zahouani et al. "Remote sensing imagery segmentation in object-based analysis: A review of methods, optimization, and quality evaluation over the past 20 years". In: *Remote Sensing Applications: Society and Environment* 32 (2023), p. 101031. ISSN: 2352-9385. DOI: https://doi.org/10.1016/j.rsase.2023.101031. URL: https://www.sciencedirect.com/science/article/pii/S2352938523001131.

# Arivis Cloud Measurement .csv Headers

file_name

well_id

bbox_y_start

bbox_y_end

centroid_y

convex_area

equivalent_diameter_um

filled_area_um2

minor_axis_length_um

solidity

class_name

object_id

bbox_y_start_um

bbox_y_end_um

centroid_y_um

convex_area_um2

euler_number

major_axis_length

orientation

time

area

bbox_x_start

bbox_x_end

centroid_x

eccentricity

extent

major_axis_length_um

perimeter

z

area_um2

bbox_x_start_um

bbox_x_end_um

centroid_x_um

equivalent_diameter

filled_area

minor_axis_length

perimeter_um

# Bright25-bestv2 Segmentations
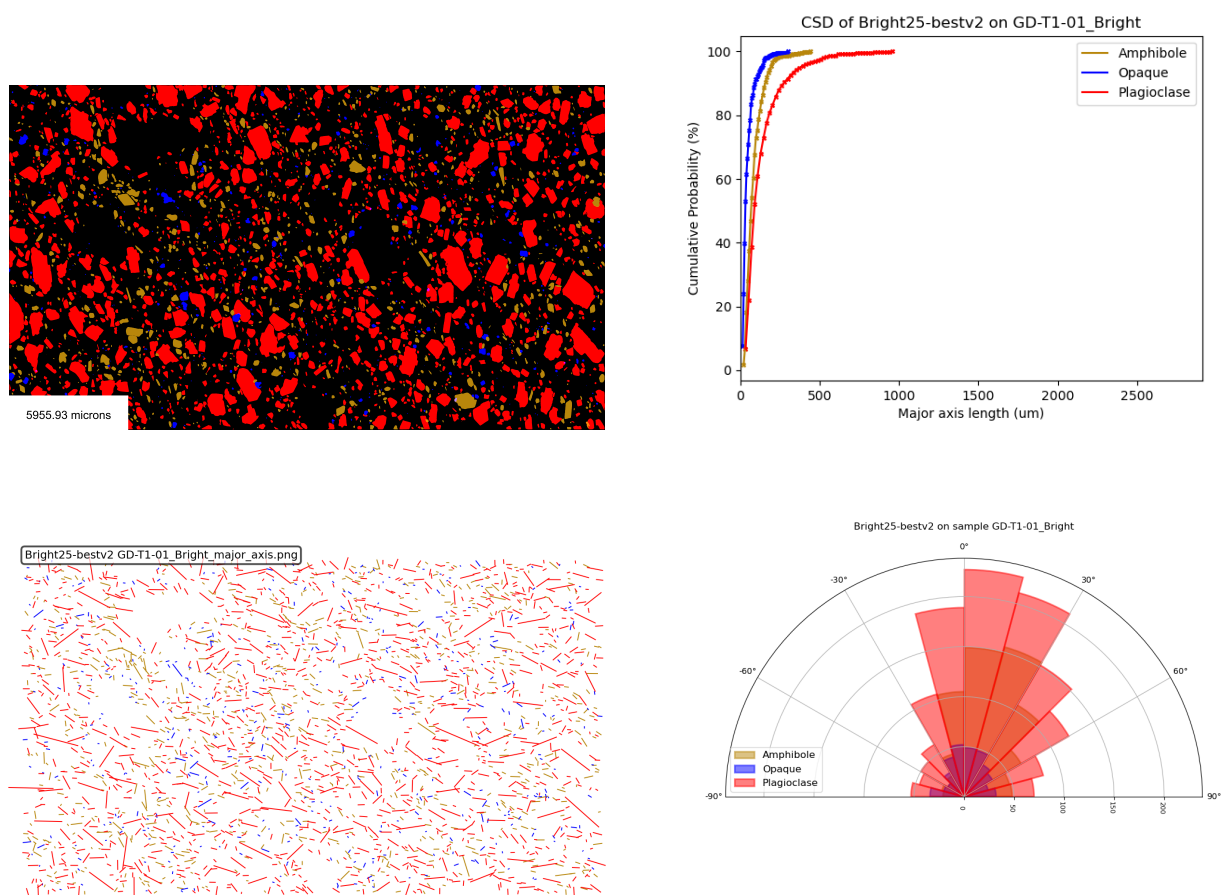


**Figure B.1:** Output data for sample GD-T1-01 under BL segmented with model Bright25-bestv2. Dark goldenrod, blue, and red are amphiboles, opaque minerals, and plagioclase respectively.
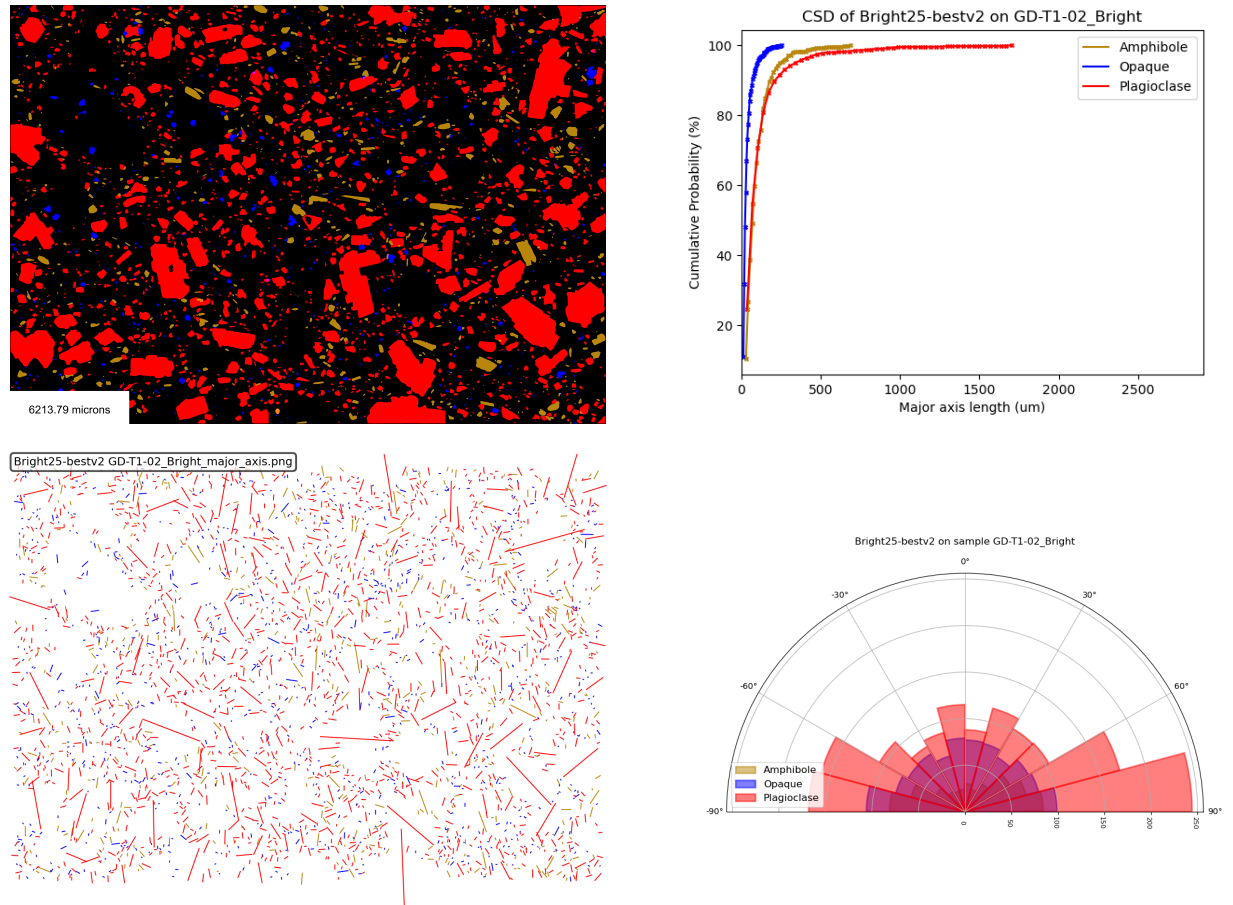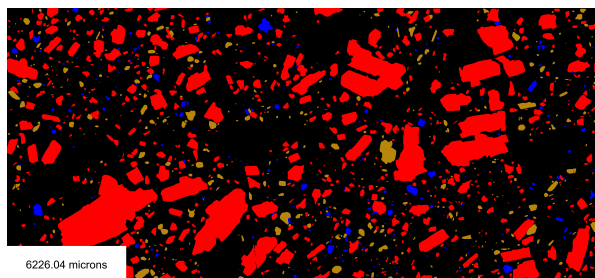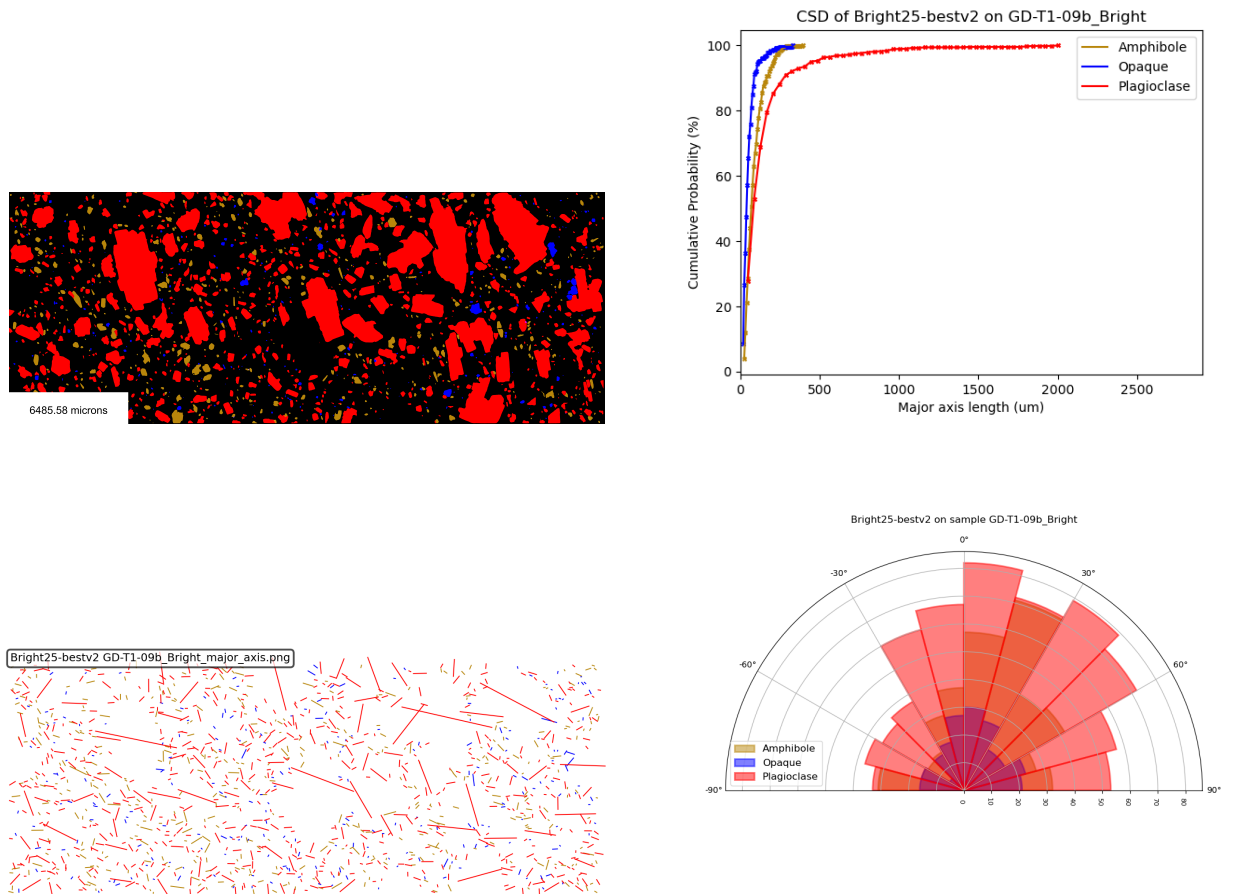
**Figure B.2:** Output data for sample GD-T1-02 under BL segmented with model Bright25-bestv2. Dark goldenrod, blue, and red are amphiboles, opaque minerals, and plagioclase respectively.
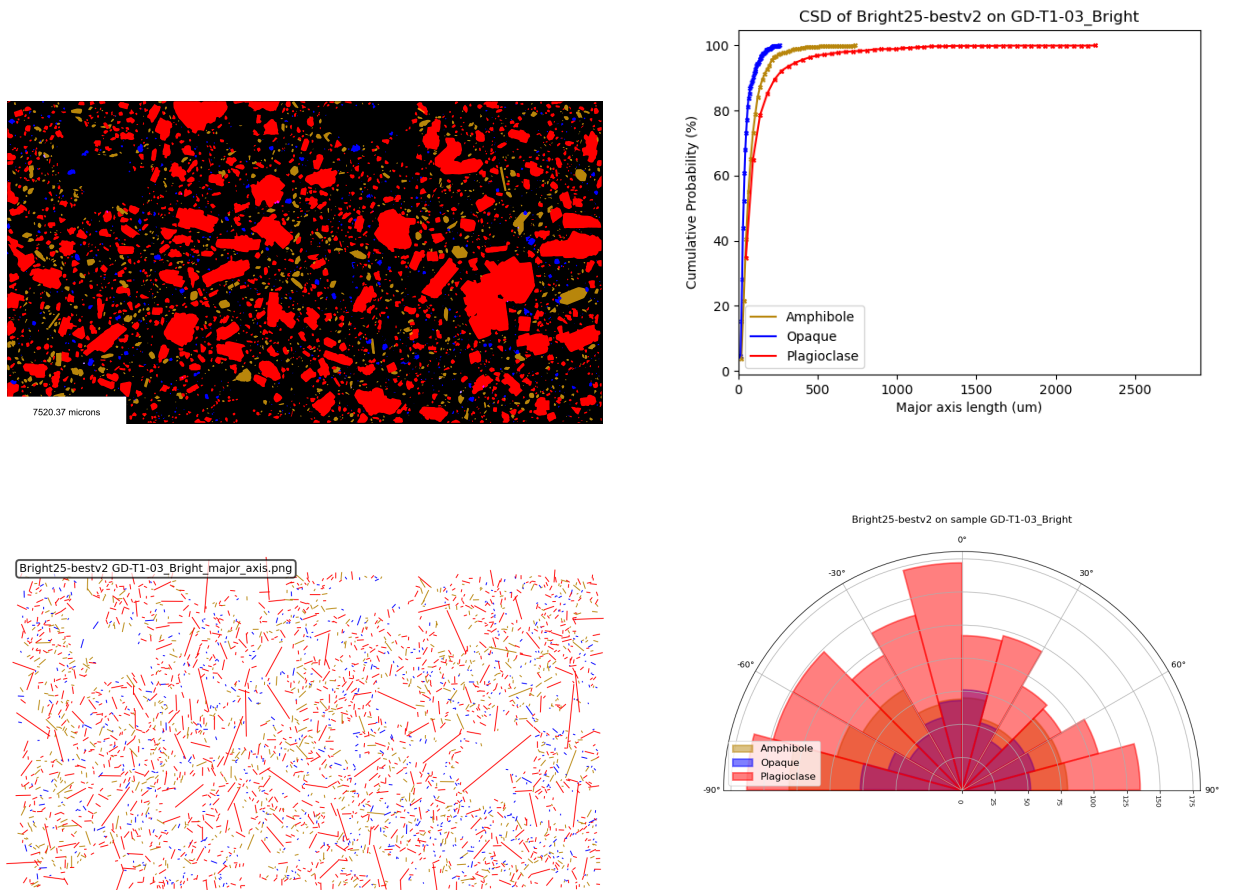
**Figure B.3:** Output data for sample GD-T1-03 under BL segmented with model Bright25-bestv2. Dark goldenrod, blue, and red are amphiboles, opaque minerals, and plagioclase respectively.
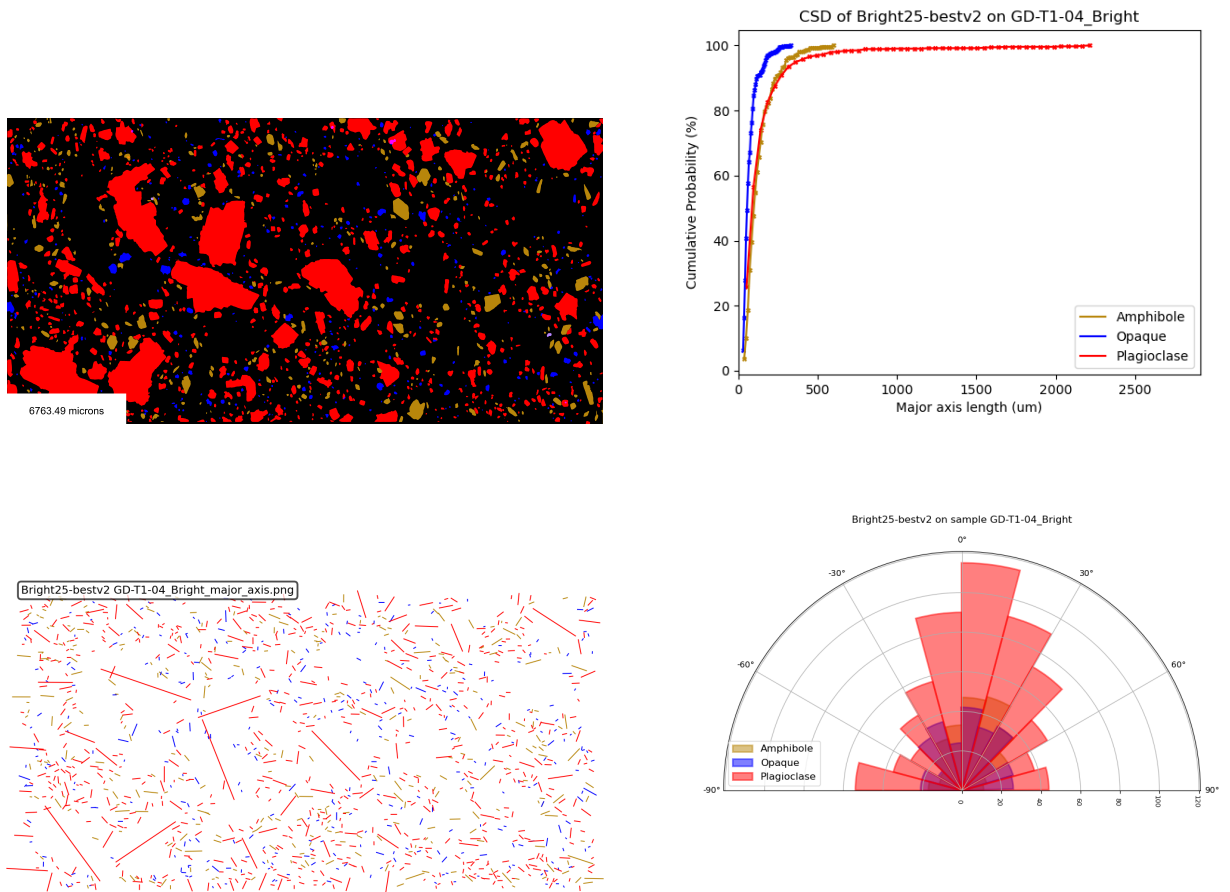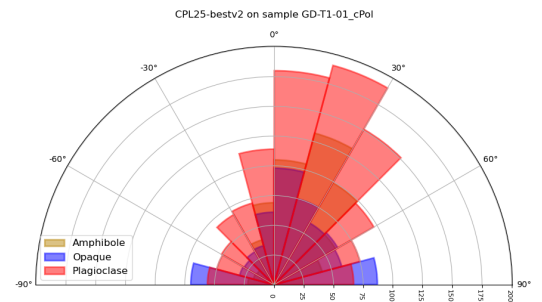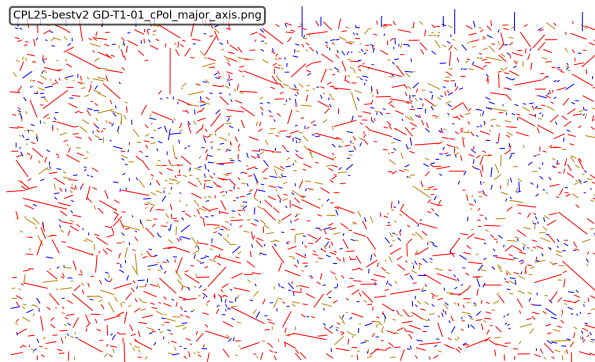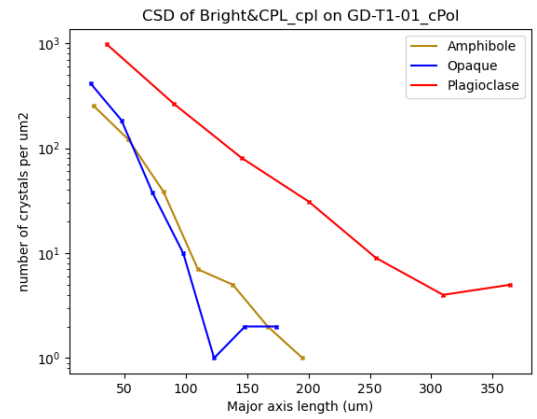
**Figure B.4:** Output data for sample GD-T1-04 under BL segmented with model Bright25-bestv2. Dark goldenrod, blue, and red are amphiboles, opaque minerals, and plagioclase respectively.
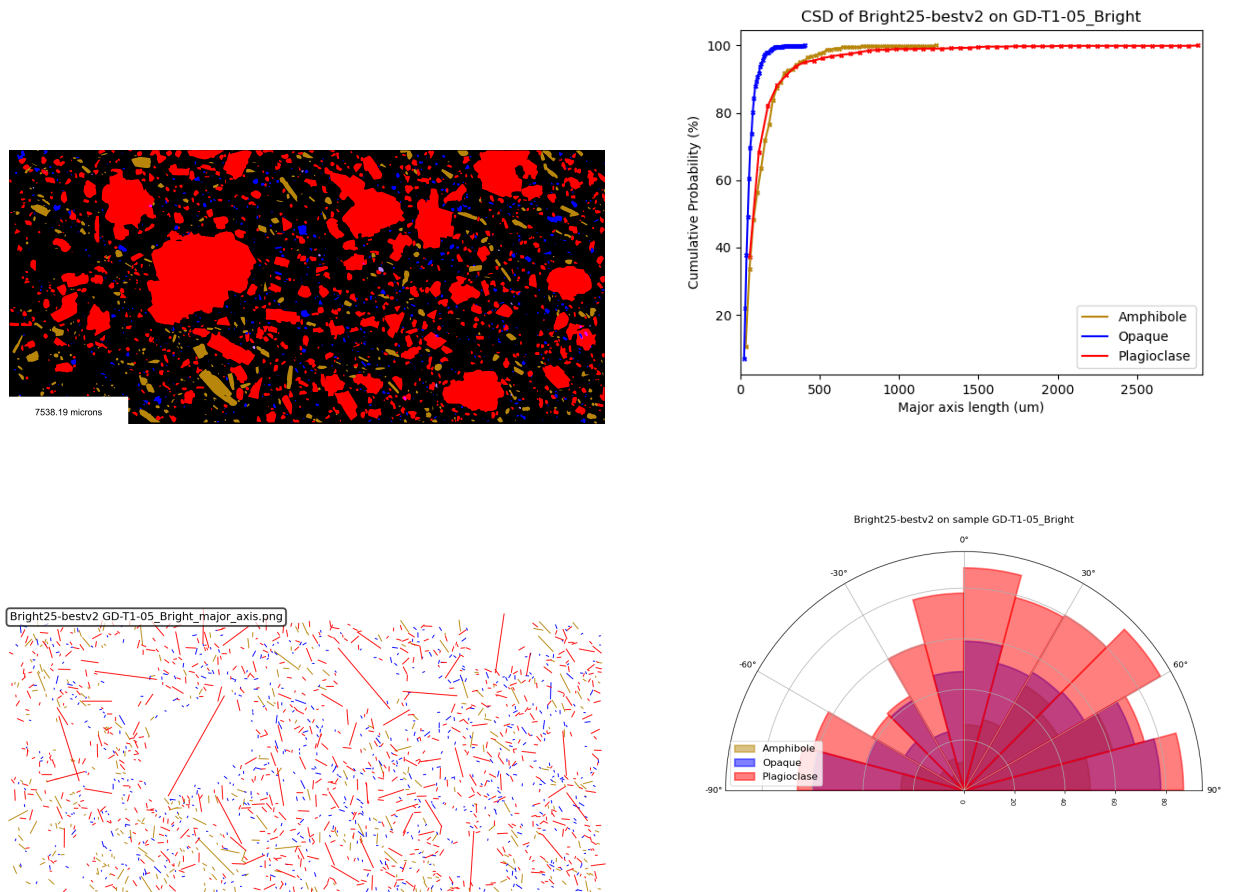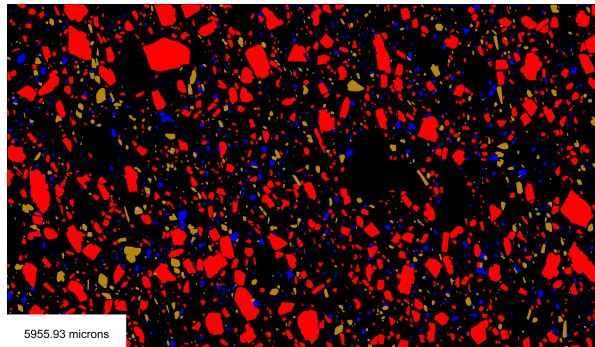
**Figure B.5:** Output data for sample GD-T1-05 under BL segmented with model Bright25-bestv2. Dark goldenrod, blue, and red are amphiboles, opaque minerals, and plagioclase respectively.
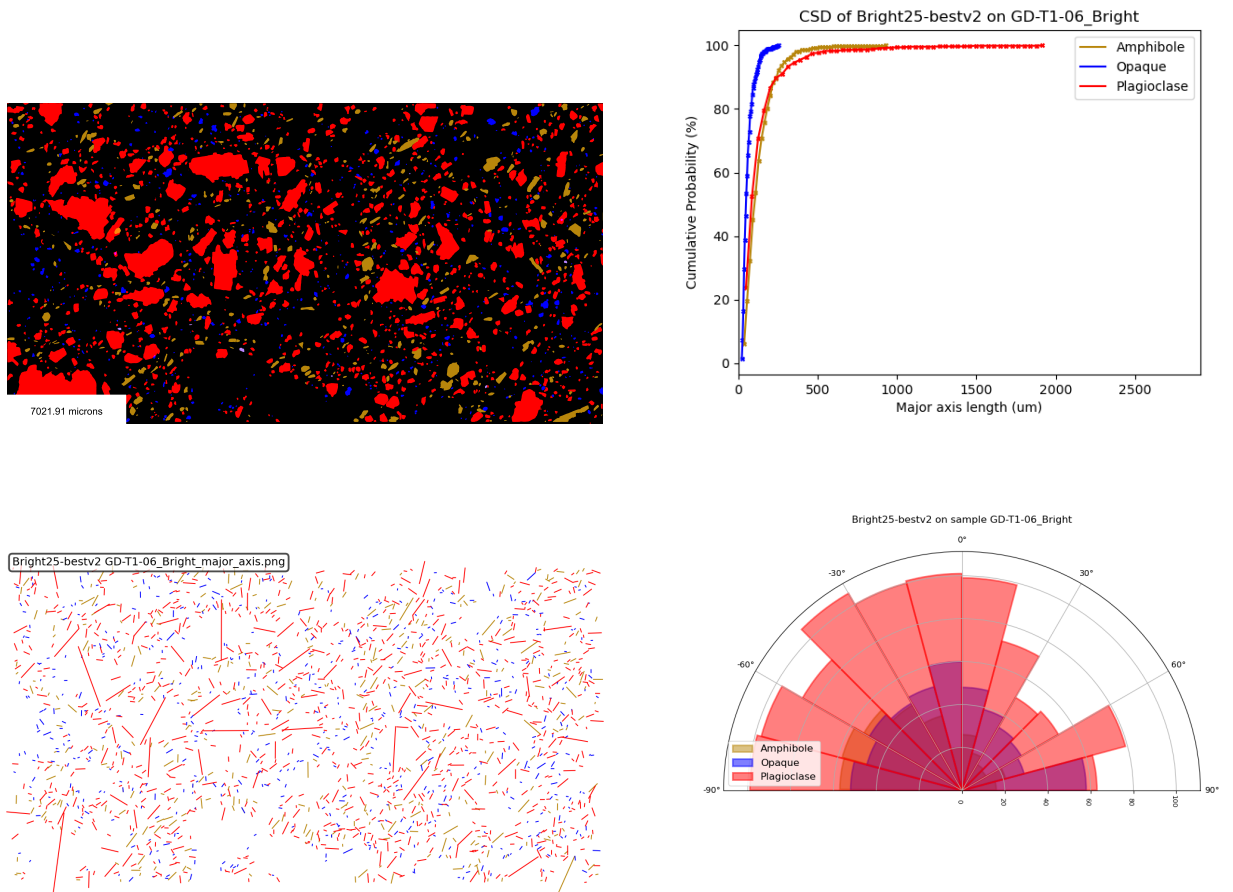
**Figure B.6:** Output data for sample GD-T1-06 under BL segmented with model Bright25-bestv2. Dark goldenrod, blue, and red are amphiboles, opaque minerals, and plagioclase respectively.
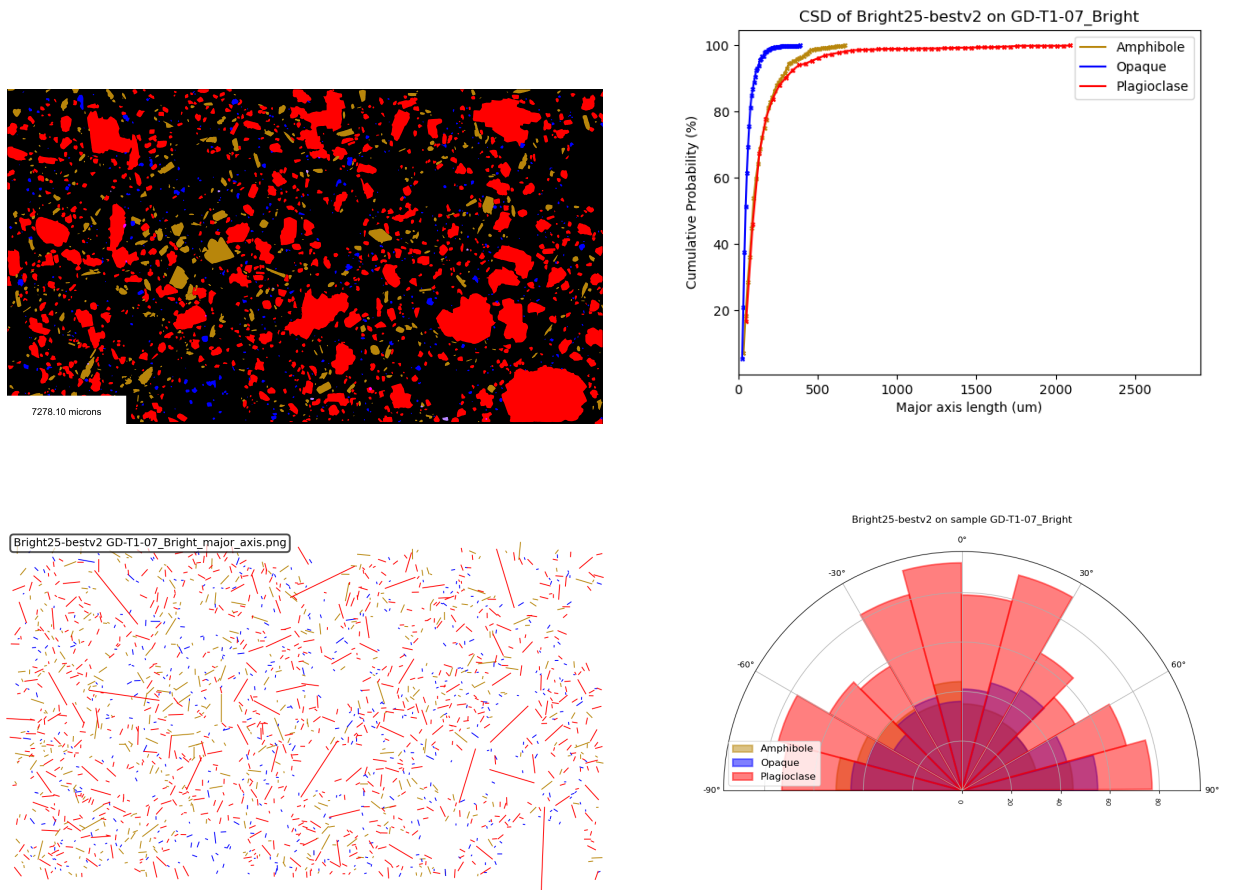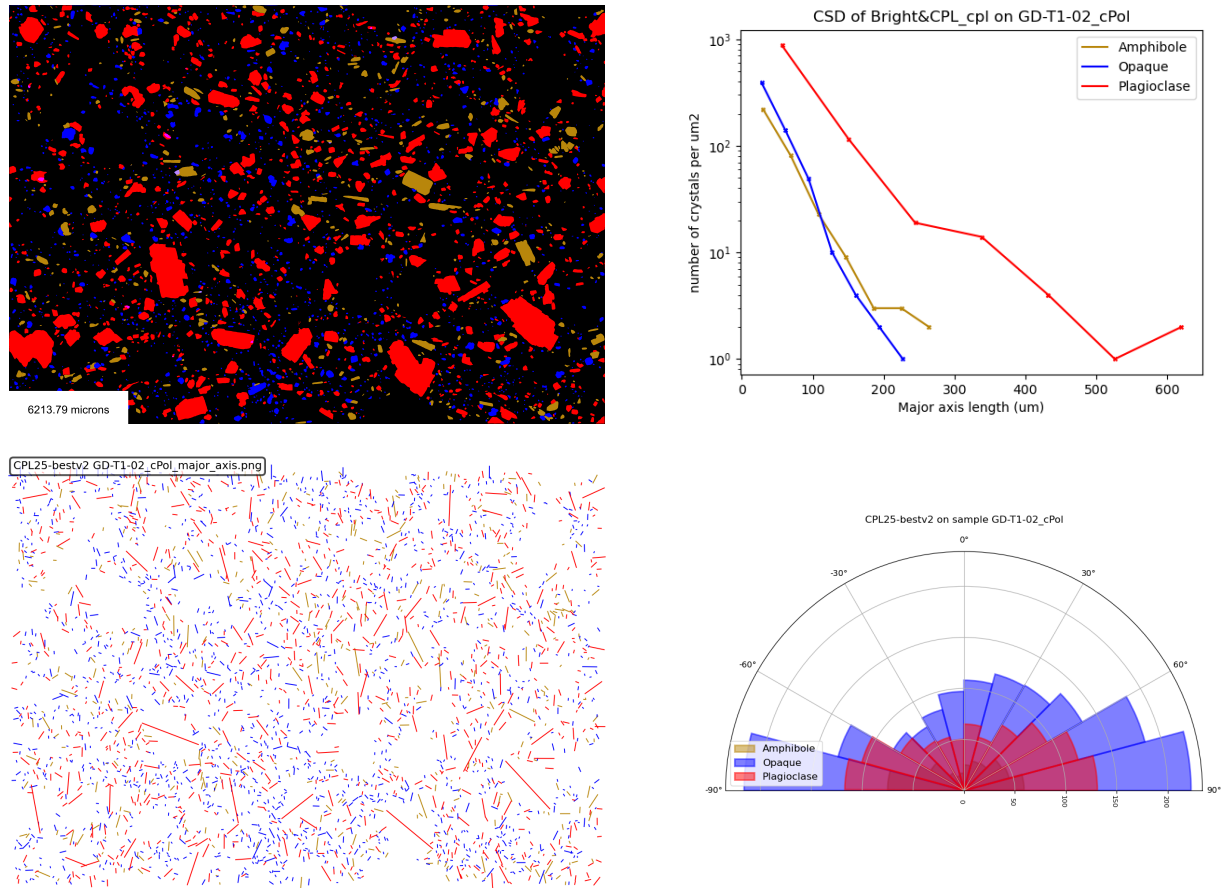
**Figure B.7:** Output data for sample GD-T1-07 under BL segmented with model Bright25-bestv2. Dark goldenrod, blue, and red are amphiboles, opaque minerals, and plagioclase respectively.
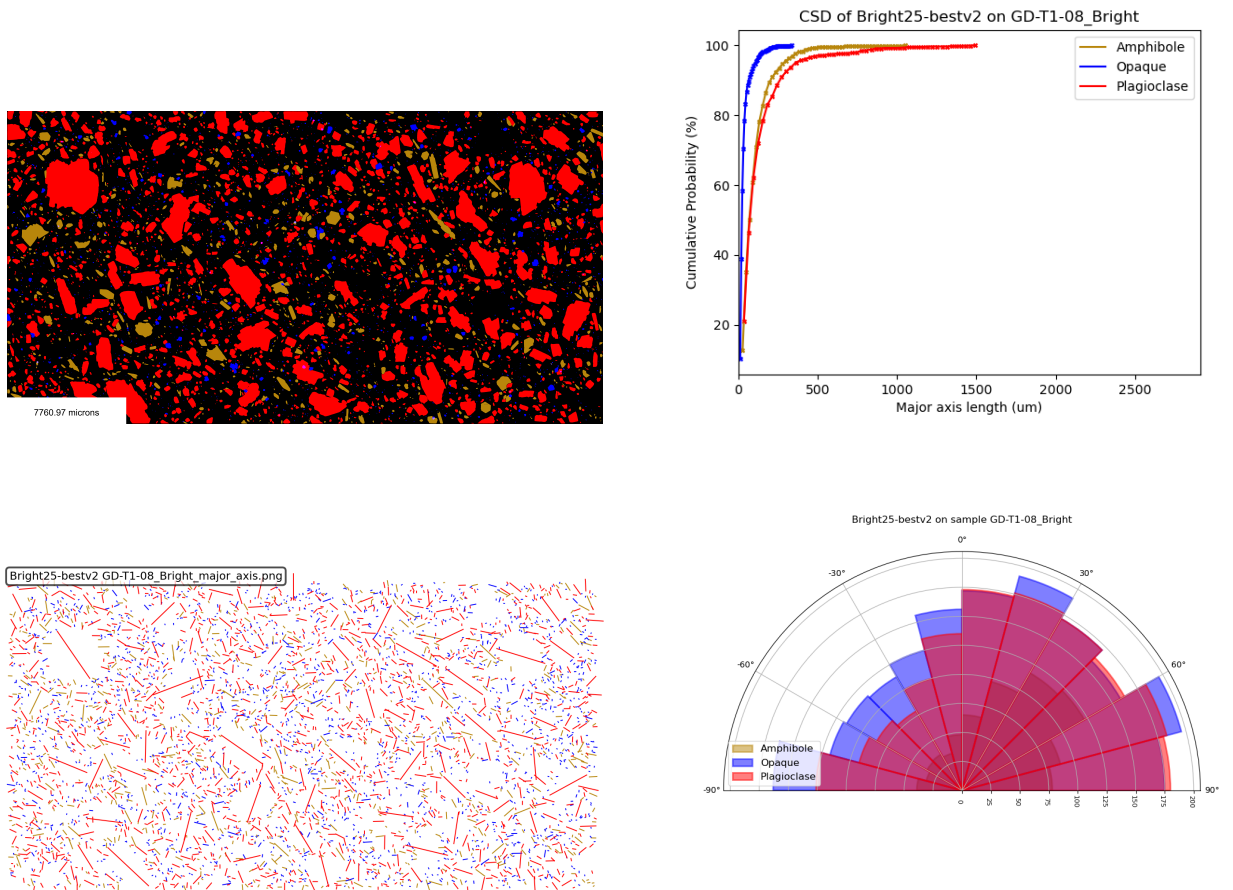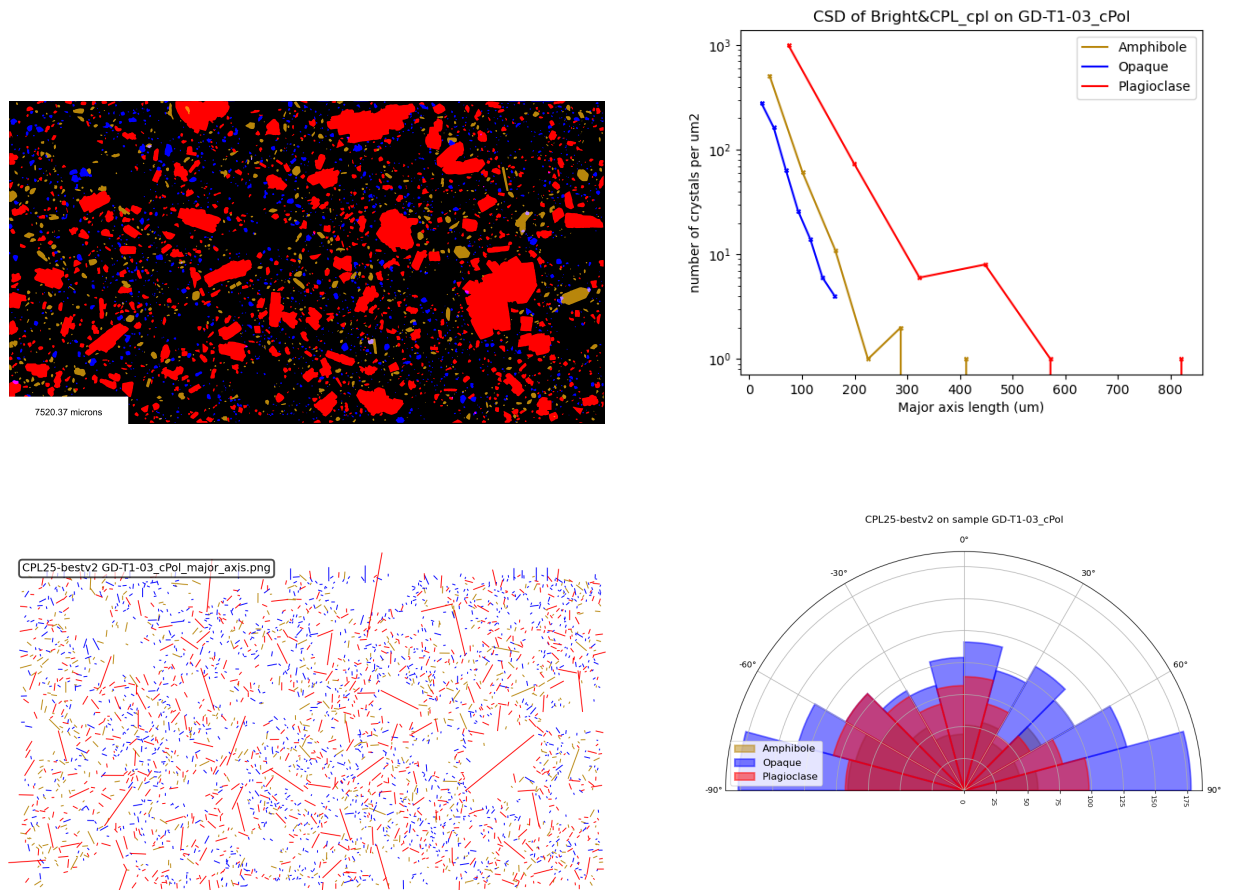
**Figure B.8:** Output data for sample GD-T1-08 under BL segmented with model Bright25-bestv2. Dark goldenrod, blue, and red are amphiboles, opaque minerals, and plagioclase respectively.
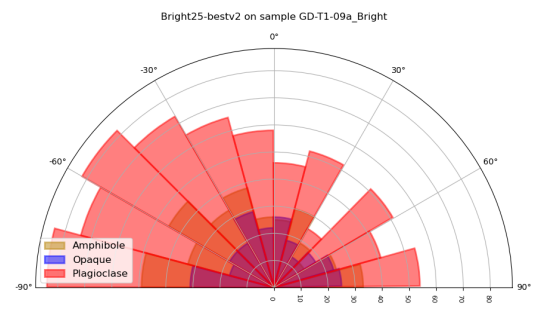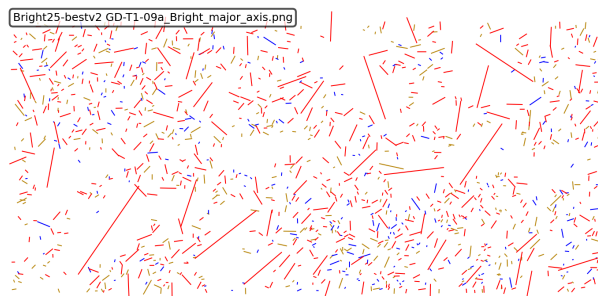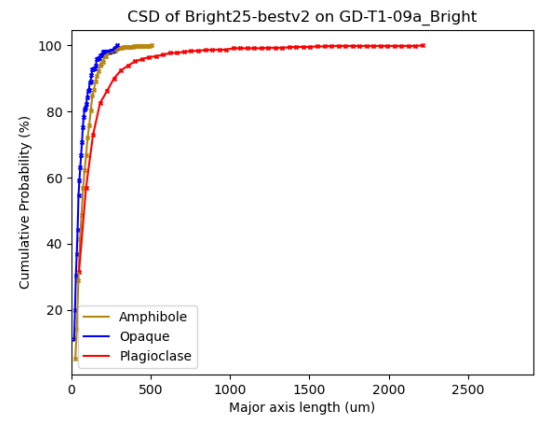
**Figure B.9:** Output data for sample GD-T1-09a under BL segmented with model Bright25-bestv2. Dark goldenrod, blue, and red are amphiboles, opaque minerals, and plagioclase respectively.

**Figure B.10:** Output data for sample GD-T1-09b under BL segmented with model Bright25-bestv2. Dark goldenrod, blue, and red are amphiboles, opaque minerals, and plagioclase respectively.

# CPL25-bestv2 Segmentations





**Figure C.1:** Output data for sample GD-T1-01 under CPL segmented with model CPL25-bestv2. Dark goldenrod, blue, and red are amphiboles, opaque minerals, and plagioclase respectively.
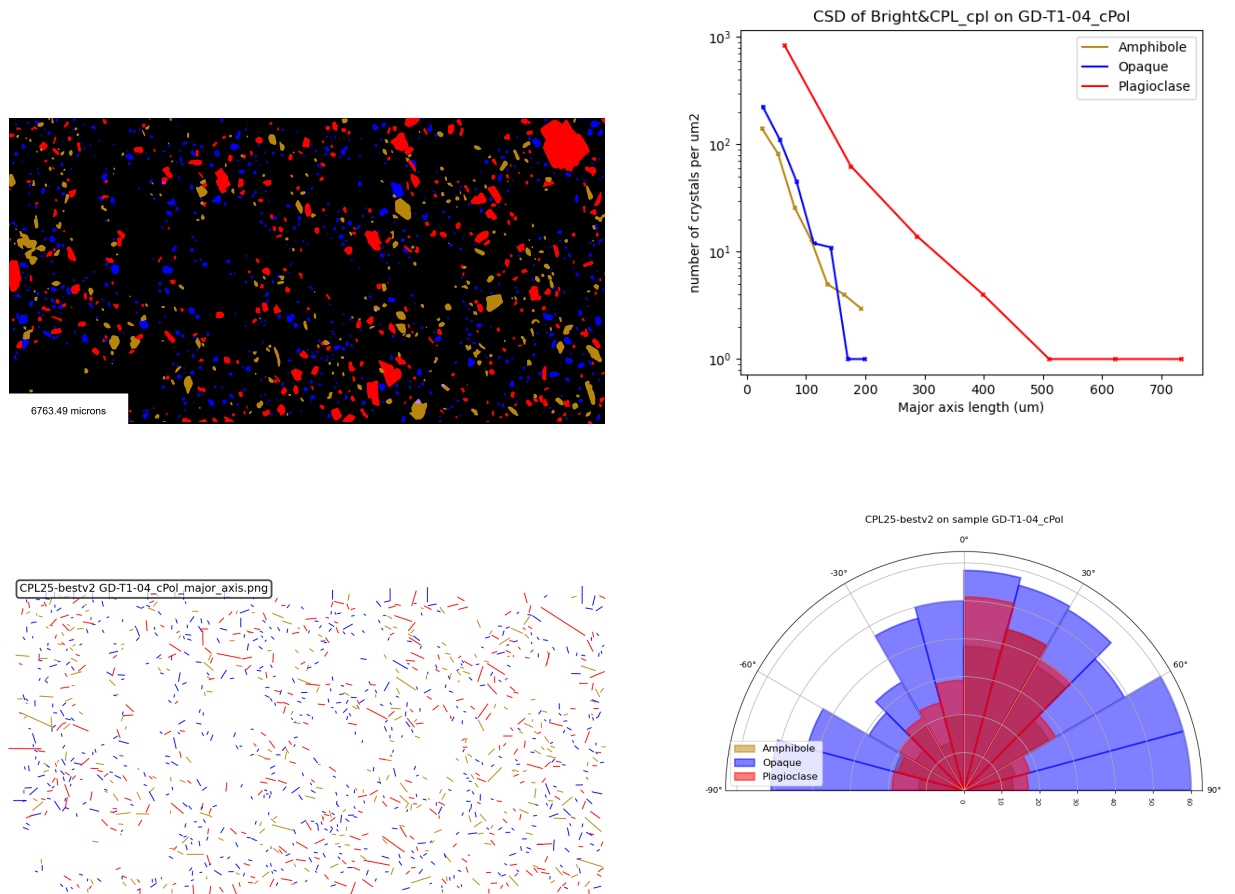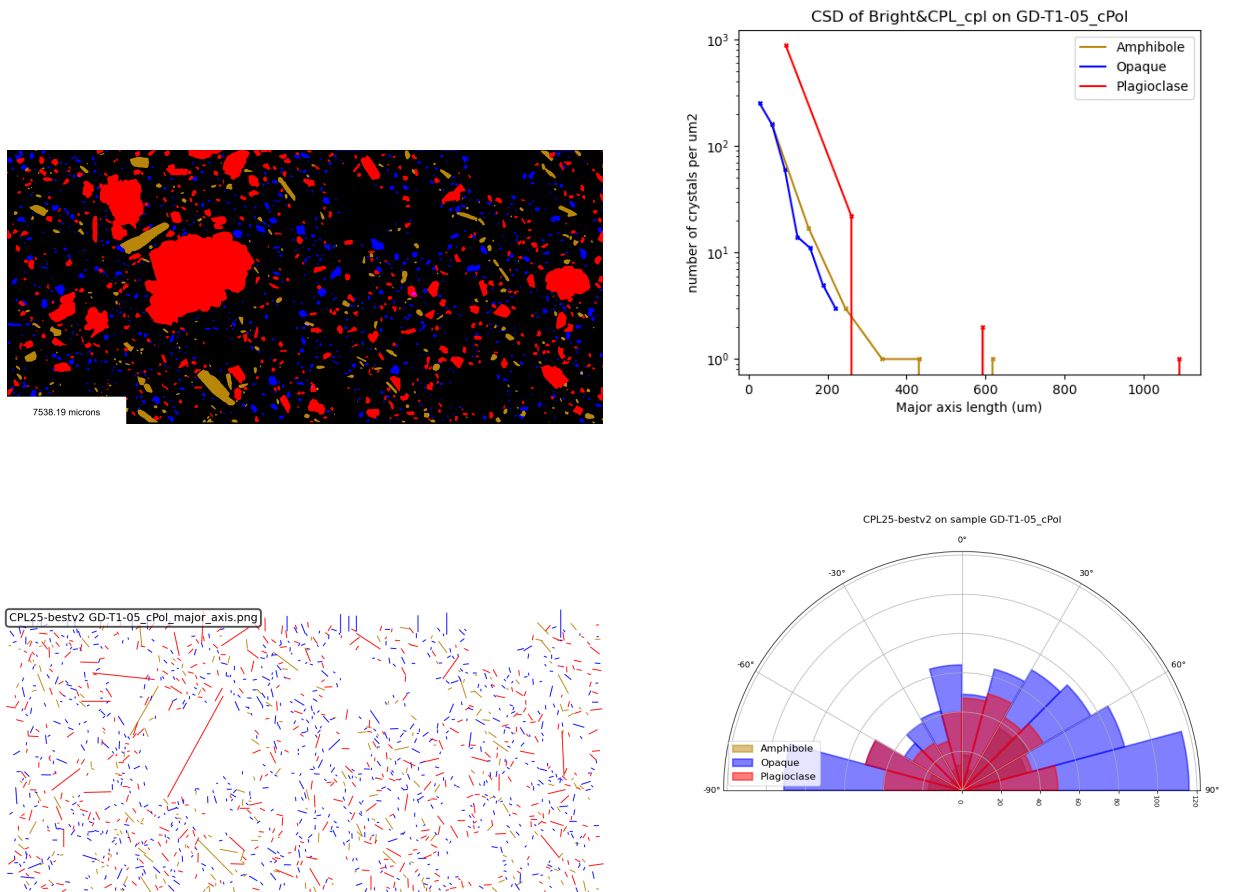
**Figure C.2:** Output data for sample GD-T1-02 under CPL segmented with model CPL25-bestv2. Dark goldenrod, blue, and red are amphiboles, opaque minerals, and plagioclase respectively.
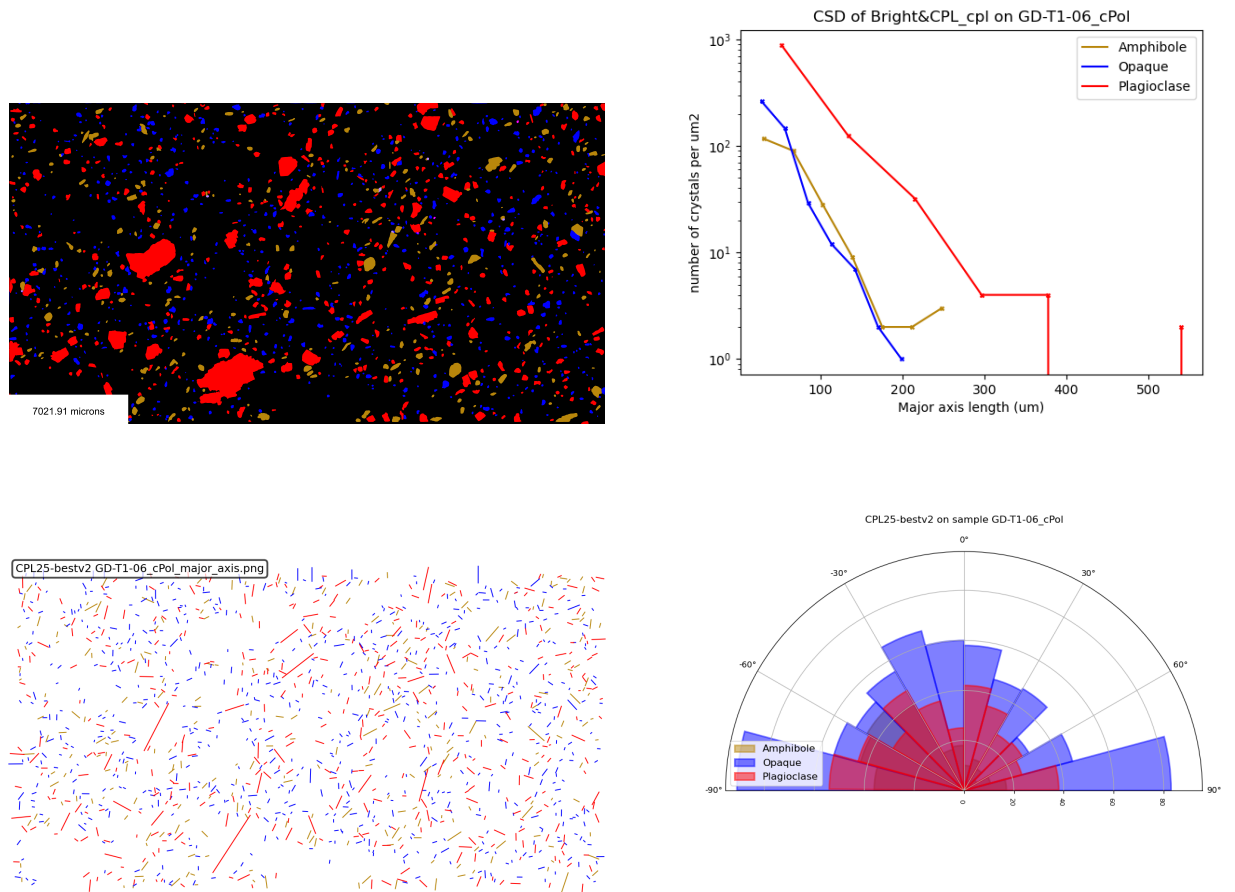
**Figure C.3:** Output data for sample GD-T1-03 under CPL segmented with model CPL25-bestv2. Dark goldenrod, blue, and red are amphiboles, opaque minerals, and plagioclase respectively.
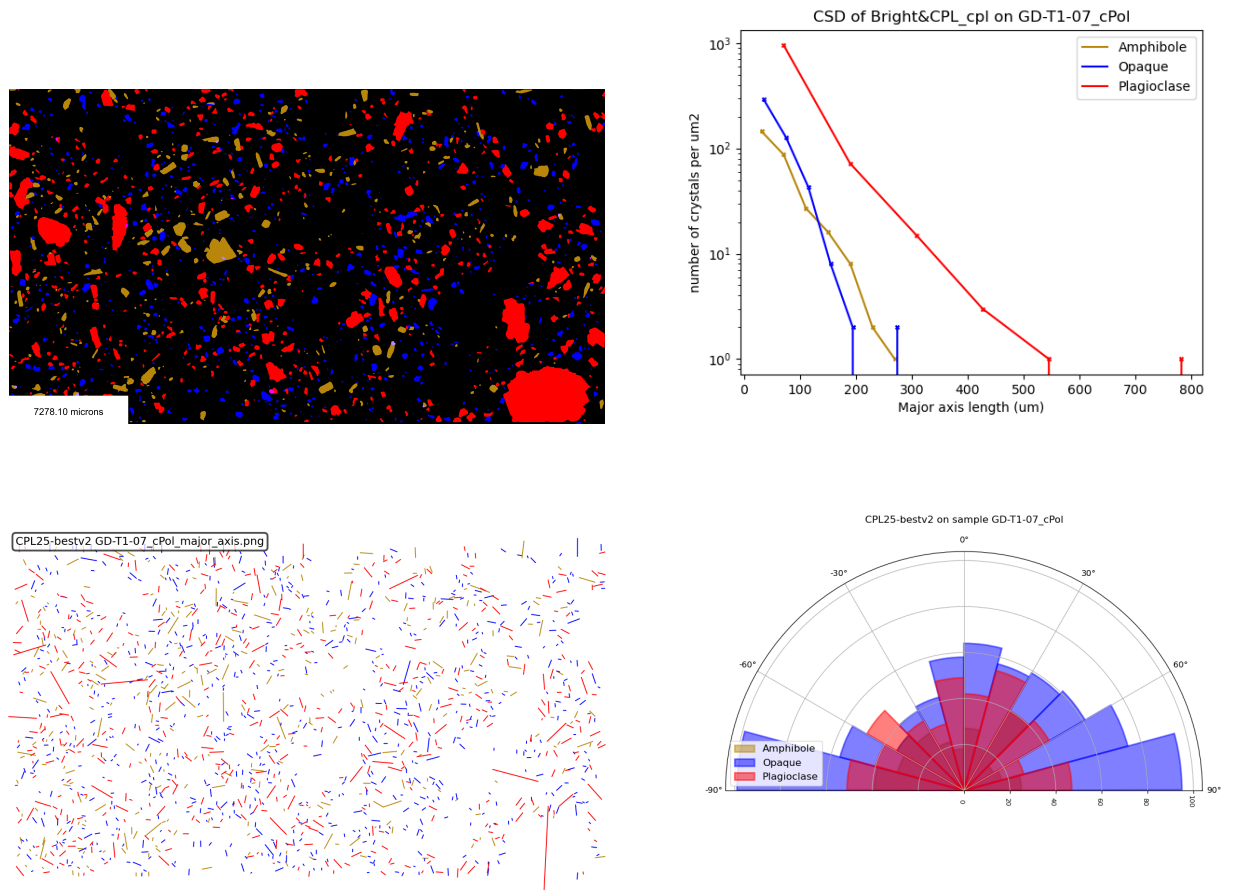
Figure C.4: Output data for sample GD-T1-04 under CPL segmented with model CPL25-bestv2. Dark goldenrod, blue, and red are amphiboles, opaque minerals, and plagioclase respectively.

**Figure C.5:** Output data for sample GD-T1-05 under CPL segmented with model CPL25-bestv2. Dark goldenrod, blue, and red are amphiboles, opaque minerals, and plagioclase respectively.

Figure C.6: Output data for sample GD-T1-06 under CPL segmented with model CPL25-bestv2. Dark goldenrod, blue, and red are amphiboles, opaque minerals, and plagioclase respectively.

**Figure C.7:** Output data for sample GD-T1-07 under CPL segmented with model CPL25-bestv2. Dark goldenrod, blue, and red are amphiboles, opaque minerals, and plagioclase respectively.
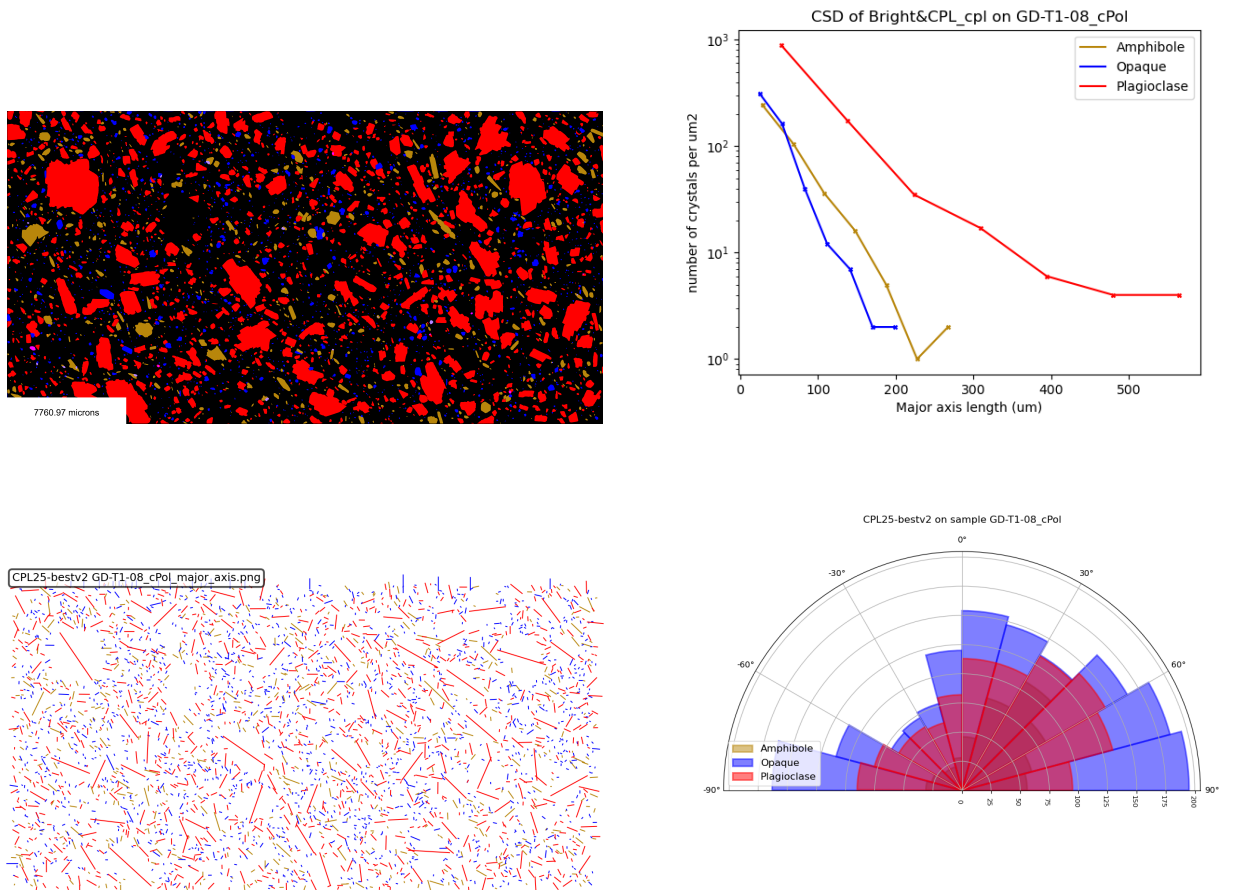
**Figure C.8:** Output data for sample GD-T1-08 under CPL segmented with model CPL25-bestv2. Dark goldenrod, blue, and red are amphiboles, opaque minerals, and plagioclase respectively.
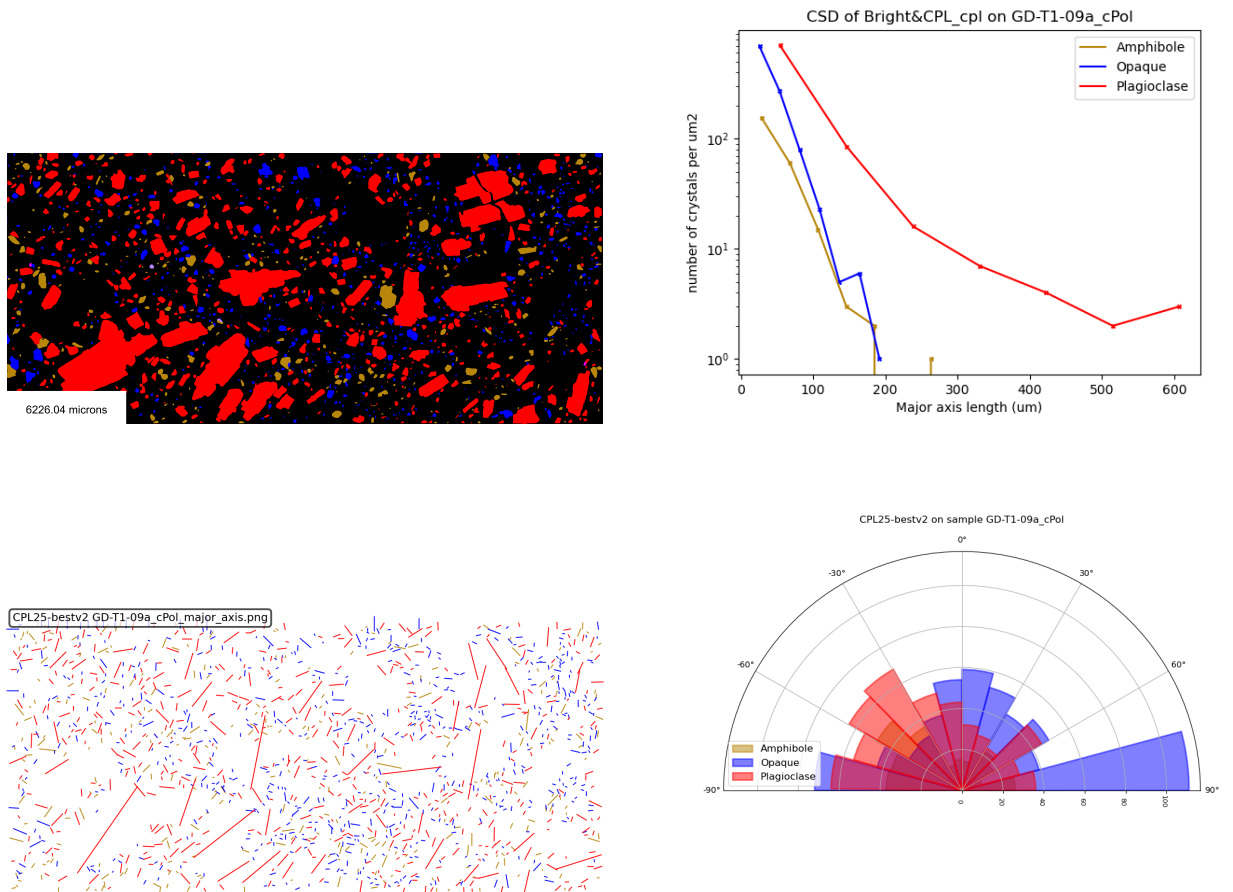
**Figure C.9:** Output data for sample GD-T1-09a under CPL segmented with model CPL25-bestv2. Dark goldenrod, blue, and red are amphiboles, opaque minerals, and plagioclase respectively.
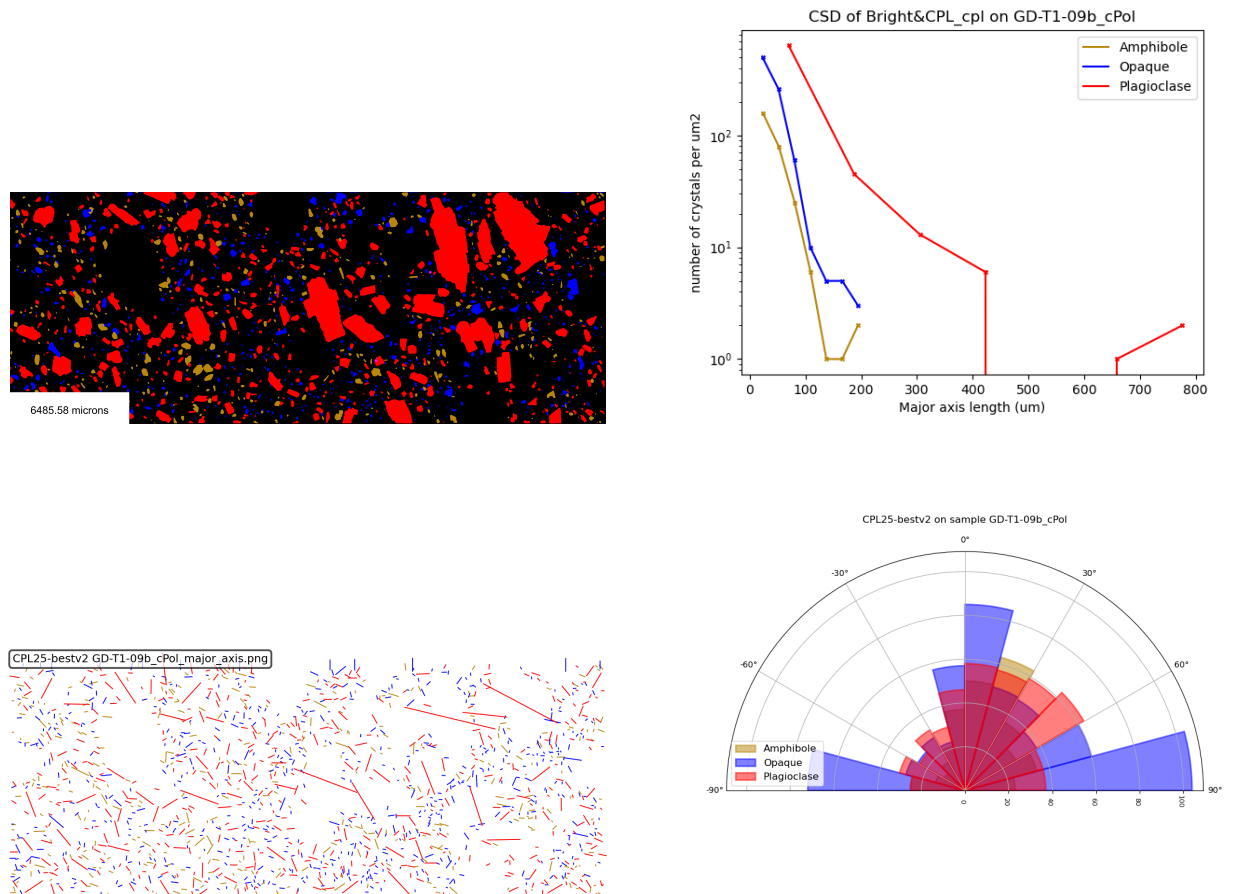
**Figure C.10:** Output data for sample GD-T1-09b under CPL segmented with model CPL25-bestv2. Dark goldenrod, blue, and red are amphiboles, opaque minerals, and plagioclase respectively.